



Investigation of transition metal-doped $\text{BaCe}_{0.8}\text{Y}_{0.2}\text{O}_{3-\delta}$ cathodes for protonic ceramic fuel cells: Microstructural and electrical properties

Amir Sultan^{a,b}, Michał Gogacz^b, Jakub Lach^b, Richard T. Baker^c, Muhammad Ali Khalid^d, Yihan Ling^e, Kun Zheng^{b,e,f,*} 

^a Jerzy Haber Institute of Catalysis and Surface Chemistry, Polish Academy of Sciences, Niezapominajek 8, PL-30239 Krakow, Poland

^b Faculty of Energy and Fuels, AGH University of Krakow, al. A. Mickiewicza 30, 30-059 Krakow, Poland

^c EaStChem School of Chemistry, University of St Andrews, St Andrews, Fife, UK

^d State Key Laboratory of Multiphase Flow in Power Engineering, School of Energy and Power Engineering, Xi'an Jiaotong University, Xian 710049, PR China

^e School of Materials Science and Physics, China University of Mining and Technology, Xuzhou, 221116, PR China

^f AGH Centre of Energy, AGH University of Krakow, ul. Czarnowiejska 36, 30-054 Krakow, Poland

ARTICLE INFO

Keywords:

Protonic ceramic fuel cells
Oxygen electrode
Proton-conducting
transition metal-doping in $\text{BaCe}_{0.8}\text{Y}_{0.2}\text{O}_{3-\delta}$

ABSTRACT

Protonic ceramic cathodes have emerged as a vital component for enhancing the efficiency and performance of protonic ceramic fuel cells (PCFCs) due to their excellent protonic conductivity and intermediate operation temperature. In this work, the doping effect of transition metals in $\text{BaCe}_{0.8}\text{X}_{0.1}\text{Y}_{0.1}\text{O}_{3-\delta}$ (X = Ni, Co, and Cu, BCXY) perovskites was systematically investigated. The phase analysis via X-ray diffraction (XRD) studies confirmed the development of single-phase perovskite for all doped samples. Transmission electron microscopy (TEM) and Scanning electron microscopy (SEM) were employed to examine the surface morphology, revealing clear and well-defined crystallites. TEM mapping further demonstrated the uniform dispersion of dopants, indicating successful synthesis. X-ray photoelectron spectroscopy (XPS) further validates the elemental composition and purity of the samples. The lowest area-specific resistance (ASR) values were obtained for BCCuY at 750 °C, measuring $0.21 \Omega\text{-cm}^2$ in dry air and $0.17 \Omega\text{-cm}^2$ in wet air. The activation energies in wet air atmosphere were found to be in the order of BCCuY (0.64 eV) < BCCoY (0.76 eV) < BCNiY (1.12 eV), within the temperature range of 600 to 750 °C, suggesting that BCCuY has the lowest activation energy and potentially better catalytic activity in these conditions. Considering these results, BCCuY perovskite shows promise as a protonic ceramic cathode for PCFCs. The long-term chemical compatibility evaluation was performed at 800 °C for 100 hrs, which showed that all three electrode materials are chemically compatible with BCZY electrolyte. This work shows the strategy of doping transition metals in $\text{BaCeO}_{3-\delta}$ -type oxides could be of great interest for the successful development of novel oxygen electrodes for PCFCs.

1. Introduction

Solid oxide fuel cells (SOFCs) are environmentally friendly and highly efficient devices that convert a wide variety of fuels, such as biogas, natural gas, and hydrogen directly to electricity. Due to their low CO_2 emissions, SOFCs are among the cleanest technologies [1]. Research on SOFCs has been conducted across the world. However, high cost and materials compatibility are challenging due to the required high operation temperature. Therefore, a lot of efforts have been made to construct low and intermediate-temperature range SOFCs [2–4]. Based on the charge carriers facilitated by the ion moment in the electrolyte,

SOFCs are classified into two main categories: protonic ceramic fuel cells (PCFCs) and oxygen ion-conducting SOFCs (O-SOFCs). In O-SOFCs, the primary charge carriers are oxygen ions (O^{2-}) while the charge carriers in PCFCs are proton ions (H^+). Compared to O-SOFCs, the PCFCs are more suitable to operate at low and intermediate temperatures due to the smaller activation energy required for the diffusion of proton ions, as the size of proton ions is smaller than oxygen ions. Additionally, the water formation takes place at the anode in O-SOFCs which dilutes the fuel. While in PCFCs, the water produced at the cathode prevents the fuel's dilution resulting in enhancing the fuel utilization and overall performance [5,6]. Developing suitable electrode materials for PCFCs is

* Corresponding author.

E-mail address: zheng@agh.edu.pl (K. Zheng).

<https://doi.org/10.1016/j.electacta.2025.146127>

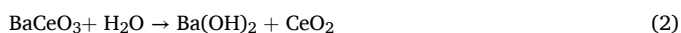
Received 28 November 2024; Received in revised form 9 March 2025; Accepted 27 March 2025

Available online 29 March 2025

0013-4686/© 2025 Elsevier Ltd. All rights reserved, including those for text and data mining, AI training, and similar technologies.

always a challenge, as the PCFCs operate at low temperatures, causing a significant increase in the cathode's polarization resistance [7]. The high polarization resistance limits the performance of the cell. To design high-performance cathode materials for PCFCs, two key aspects are pivotal: ensuring the efficient transport of both oxygen and proton ions within the cathode materials and enhancing the ORR activity at low temperatures. The introduction of dual proton and oxygen ions conductivities into the cathode materials increases the active sites which has a direct effect on enhancing ORR activity [8].

In the recent decade, BaCeO₃-based materials have attracted worldwide attention due to their potential application in PCFCs. At low temperatures, BaCeO₃-based oxides possess high proton conductivity in the presence of humid hydrogen [9–11]. Therefore, BaCeO₃ doped with transition metals can be applied as electrode candidates for PCFCs. However, the BaCeO₃ core material exhibits poor chemical stability in the presence of atmospheric containing CO₂ and H₂O. Which limits such materials from being used in future SOFC applications [11]. The chemical reactions of BaCeO₃ with the atmosphere containing CO₂ and H₂O are:



To overcome the problems discussed above, researchers are using different approaches, either by making composite electrodes of BaCeO₃-based materials or doping some transition metals in BaCeO₃ to improve the performance of electrode materials for fuel cells. Significant research work has been done to develop novel oxygen electrode materials for PCFCs to enhance the performance of oxygen reduction reaction (ORR) and lower polarization resistance at low temperatures [12].

Sun et al. [13] fabricated a composite of BaCe_{0.8}Sm_{0.2}O_{3-δ} with Ce_{0.8}Sm_{0.2}O_{2-δ} and reported that the final composite has better chemical stability and smaller electronic conductivity compared to the pure BaCe_{0.8}Sm_{0.2}O_{3-δ} and Ce_{0.8}Sm_{0.2}O_{2-δ} respectively. The stability of the composite (BaCe_{0.8}Sm_{0.2}O_{3-δ}-Ce_{0.8}Sm_{0.2}O_{2-δ}) is improved because Ce_{0.8}Sm_{0.2}O_{2-δ} is used as protection from corrosion due to H₂O and CO₂ for BaCe_{0.8}Sm_{0.2}O_{3-δ}, and the lower electronic conductivity is due to the reduction of Ce_{0.8}Sm_{0.2}O_{2-δ} and electron blocking effect of BaCe_{0.8}Sm_{0.2}O_{3-δ} in the composite. Zhu et al. [14] developed and investigated a composite of BaCe_{0.8}Y_{0.2}O_{3-δ} with Ce_{0.8}Sm_{0.2}O_{2-δ} and reported that it exhibits both oxygen and hybrid proton ion conductivities. In (BaCe_{0.8}Y_{0.2}O_{3-δ}-Ce_{0.8}Sm_{0.2}O_{2-δ}) composite oxides, the oxygen ion conductivity arises due to Ce_{0.8}Sm_{0.2}O_{2-δ}, and the protonic conductivity originated from the BaCe_{0.8}Y_{0.2}O_{3-δ} perovskite oxide. Raza et al. [15] prepared Sm/Zr-doped CeO₂ (ZSDC)-K/Na₂CO₃ composite oxide and observed an ionic conductivity of 0.1 cm⁻¹ at a lower temperature of about 500 °C, and the cell's power density reached up to 700 mWcm⁻².

To enhance the overall performance of BaCeO₃-based materials, some researchers built up an idea to replace partially Ce in BaCeO₃ with single element Nb [16], Ti [17], Zr [18], In [19], etc. From these studies, it is observed that Zr-doped BaCeO₃ showed the best comprehensive performance of chemical stability and conductivity. However, the enhancement in chemical stability of Zr-doped BaCeO₃ was limited. Another serious problem is the sintering properties of BaZrO₃ materials [18]. Bi et al. [19] Doped Indium in BaCeO₃-based materials and observed enhancement in both chemical stability and the sintering performance but it had a little effect on the conductivity. When Y was doped in BaCeO₃-base materials it improved the electrical conductivity, but the chemical stability remained poor [20–22].

Medvedev et al. [23] summarized a good strategy to enhance the overall electrochemical performances of BaCeO₃-based materials to be used in SOFCs: (i) Co-doping of BaCeO₃ by two different metals, (ii) co-doping of BaCeO₃ by non-metal and metal, and (iii) Composite with BaCeO₃ base materials in which the addition phase has high chemical stability. The co-doping approach in BaCeO₃ is prevalent, in which one

element improves chemical stability while the other element enhances the conductivity (ionic and electronic) of the perovskite structure. E.g., BaIn_{0.3-x}Y_xCe_{0.7}O_{3-δ} (x = 0, 0.1, 0.2, and 0.3) [24], BaCe_{0.7}Ta_{0.1}In_{0.2}O_{3-δ} [25] and BaCe_{0.7}Ta_{0.1}Y_{0.2}O_{3-δ} [26] expressed good performance in chemical stability against atmospheres containing H₂O and CO₂. However, the protonic and electronic conductivities are still lower.

During the last two decades, traditional cathodes designed for O-SOFCs were predominantly employed for PCFCs, e.g. Ba_{0.5}Sr_{0.5}Co_{0.8}Fe_{0.2}O_{3-δ} [27] and La_{0.6}Sr_{0.4}Co_{0.2}Fe_{0.8}O_{3-δ} [28]. Although these materials demonstrated high kinetics for the ORR in O-SOFCs as cathodes, their performance as cathodes for PCFCs has not met the desired expectations. For example, the famous cathode (Sm_{0.5}Sr_{0.5}CoO_{3-δ}) showed a much higher power density of 660 mWcm⁻² at 700 °C for O-SOFCs than 307 mWcm⁻² for PCFCs [29,30]. With continuous advancements in cathode research, nowadays specifically cathode materials are being designed for PCFCs. Duan et al. [31] designed a novel BaCo_{0.4}Fe_{0.4}Zr_{0.1}Y_{0.1}O_{3-δ} cathode which exhibits triple conductivities (electronic, oxygen, and proton ion) and demonstrated high catalytic activity in ORR for PCFCs at both low and intermediate temperatures. Kim et al. [32] developed triple-conducting NdBa_{0.5}Sr_{0.5}Co_{1.5}Fe_{0.5}O_{5+δ} as a cathode for PCFCs which showed a high-power output of 1370 mWcm⁻² at 700 °C. Xia et al. [33] co-doped Sn and Bi in BaFeO_{3-δ} material and developed BaFe_{0.5}Sn_{0.2}Bi_{0.3}O_{3-δ} as cathode for PCFCs, which showed a high peak power density of 1276 mWcm⁻² at intermediate temperature. Wei et al. [34] co-doped Ce and Y in BaFeO_{3-δ} and synthesized BaCe_{0.8}Fe_{0.1}Y_{0.1}O_{3-δ} as cathode for PCFCs, demonstrating a high-power density of 750 mW cm⁻² and low polarization resistance of 0.05 Ω cm² at 700 °C. Liang et al. [35] developed Ni-doped BaCo_{0.4}Fe_{0.4}Zr_{0.1}Y_{0.1}O_{3-δ} and Ba(Co_{0.4}Fe_{0.4}Zr_{0.1}Y_{0.1})_{0.95}Ni_{0.05}O_{3-δ} as cathode materials for both PCFCs and O-SOFCs, which exhibit high ORR activities and very low polarization resistances of 0.607 and 0.038 Ω cm² at 550 °C, respectively. A recent study by Ding et al. [36] reported that triple-conducting PrNi_{0.5}Co_{0.5}O_{3-δ} material displayed high electrochemical performance in both electrolysis and fuel cell modes as electrodes for PCFCs.

Perovskite materials, represented by a general formula ABO₃ which comprises a 3D framework, the A site is inhabited by cations of larger size such as rare earth or alkaline earth metals while the B site is inhabited by transition metals of smaller cations. The O-site depicts the oxygen anions that form octahedral coordination around the B-site. These perovskite materials are famous for the flexibility they offer in the modification of their chemical compositions. The A and B sites can be doped by different elements while the overall perovskite structure remains sustained. To date, doping has been broadly used to modify the overall (bulk and surface) properties of perovskites resulting in enhancing their physicochemical characteristics including ORR activity.

Based on the studied literature, BaCe_{0.8}Y_{0.2}O_{3-δ} (BCY) perovskite material has only ionic conductivities (O²⁻ and H⁺) and could be used as electrolyte materials. This work aims to enhance BCY by introducing electronic conductivity via doping transition metals and enabling them to be used as electrode materials for PCFCs. In this work, three transition metals Ni, Co, and Cu were doped into BaCe_{0.8}X_{0.1}Y_{0.1}O_{3-δ} perovskite, referred to as BCXY (where X = Co, Ni, or Cu), using the sol-gel method. The doping of these transition metals in BaCe_{0.8}Y_{0.2}O_{3-δ} (BCY) perovskite can possibly introduce triple conductivities. When the B-site of the perovskite is occupied by the transition metal cations, the electronic conductivity can be introduced, while the ionic conductivities (O²⁻ and H⁺) originate from the parent (BCY) perovskites. Additionally, the presence of the metal cation in perovskite, which easily changes its valence, results in high catalytic activity. The phase analysis, structural and microstructural, elemental distribution, and electrochemical properties of BCXY cathode materials were studied and explained in detail.

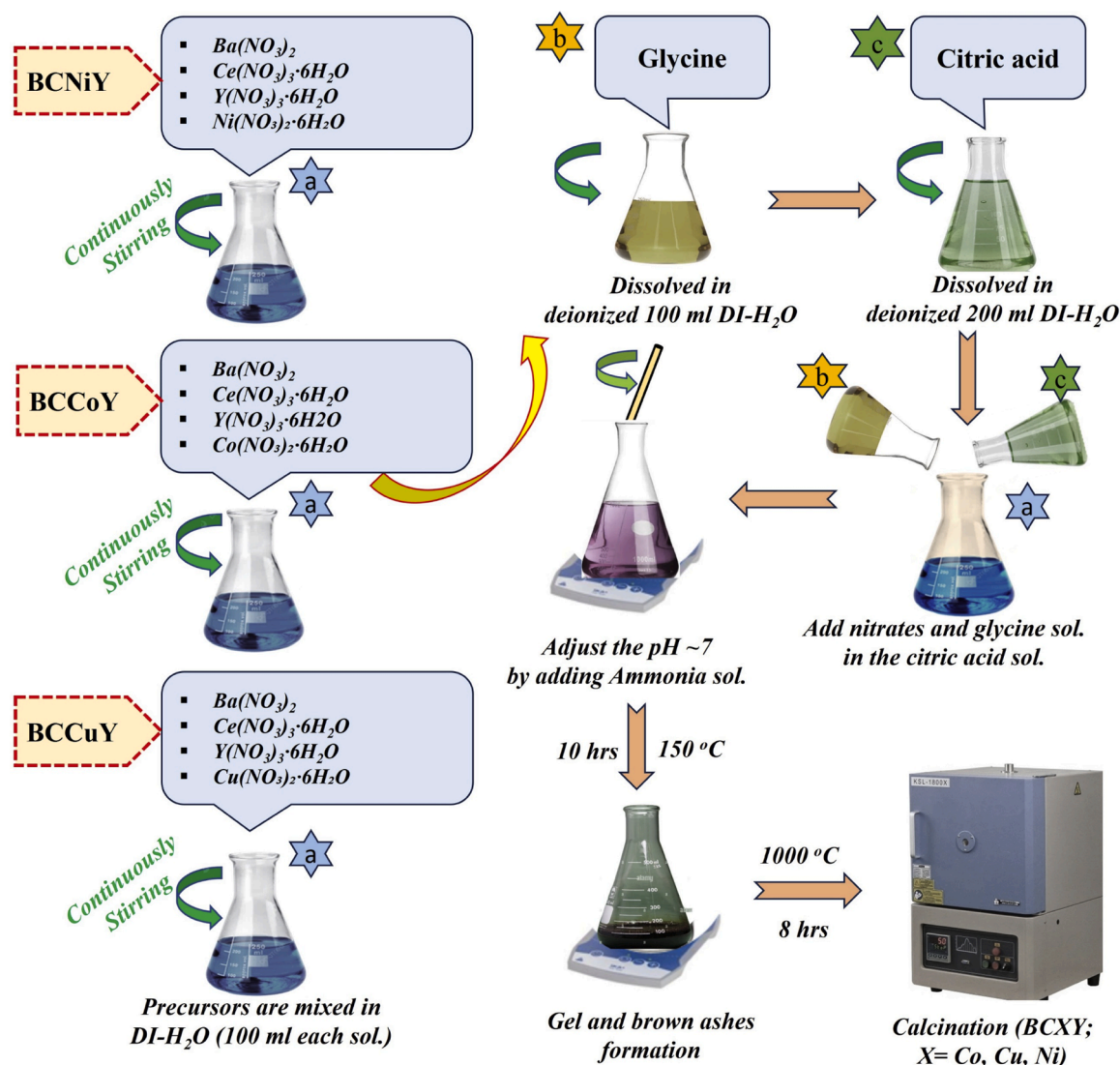


Fig. 1. Schematic illustration of obtaining $BaCe_{0.8}X_{0.1}Y_{0.1}O_{3-\delta}$ (BCXY; X=Co, Ni, and Cu) powders through the sol-gel method.

2. Experimental section

2.1. Cathode preparation

The $BaCe_{0.8}X_{0.1}Y_{0.1}O_{3-\delta}$ (BCXY; X = Ni, Co, Cu names as BCNiY, BCCoY, and BCCuY, respectively) powders were prepared using the sol-gel technique to ensure the homogeneity of the mixed nitrates. Precursors including $Ba(NO_3)_2$, $Ce(NO_3)_3 \cdot 6H_2O$, $Y(NO_3)_3 \cdot 6H_2O$, $Ni(NO_3)_2 \cdot 6H_2O$, $Co(NO_3)_2 \cdot 6H_2O$ and $Cu(NO_3)_2 \cdot 3H_2O$ were dissolved individually in deionized water, along with glycine and citric acid. These solutions were then combined with a molar ratio of 1:2:1 to ensure thorough mixing, followed by stirring for 2 h. The pH of the solution was balanced to 7 using an appropriate amount of ammonia solution. Next, the solution was heated on a stirrer at 90 °C until the water evaporated, yielding a blue viscous gel. This gel was subsequently dried in an air oven at 180 °C for 10 h to eliminate organic residues, resulting in the formation of brown ashes. Finally, the brown powders were heated in an air furnace at 1000 °C for 8 hrs to achieve complete crystallization of the BCXY perovskite structure, avoid secondary phases and decomposition, allow enough time for proper incorporation of the transition metal dopants into the BCY lattice, and obtain the proper phase homogeneity. During the calcination process, the heating and cooling rates were set to 3 °C per minute to facilitate uniform grain growth and reduce the

thermal stress. The calcined powders were then ground into fine powder using a mortar and pestle (Fig. 1).

2.2. Characterizations

X-ray diffraction (XRD) analysis was performed using a Panalytical X'Pert Pro instrument with $Cu K\alpha$ radiation ($\lambda = 1.5406 \text{ \AA}$) operated at 40 kV and 30 mA, and in a 2-theta range of 20–80° coupled with a goniometer (1/4 0.008° step size) to study the crystal structure of the BCNiY, BCCoY, and BCCuY perovskite cathode materials. The Rietveld refinement of XRD measurement was carried out using X'Pert high score plus software. Scanning field emission electron microscopy (FE-SEM) using MIRA3-TESCAN; JEOL JSM-7500 F equipment and X-ray energy dispersive spectroscopy (EDS) using INCA PentaFetx 3 equipment were performed to study the surface morphology and constituent elements of BCNiY, BCCoY, and BCCuY cathode materials. The FE-SEM and EDS equipment are coupled with each other. To prevent charging during EDS and SEM analysis a very thin layer of Au was coated to the surface of BCNiY, BCCoY, and BCCuY cathode powders. Transmission Electron Microscopy (TEM) was performed using a scanning transmission electron microscope (S/TEM) and Titan Themis 200 keV (FEI) to obtain the high-resolution (HR) TEM images and TEM-EDS mapping of BCNiY, BCCoY, and BCCuY cathode materials. The sample preparation for TEM

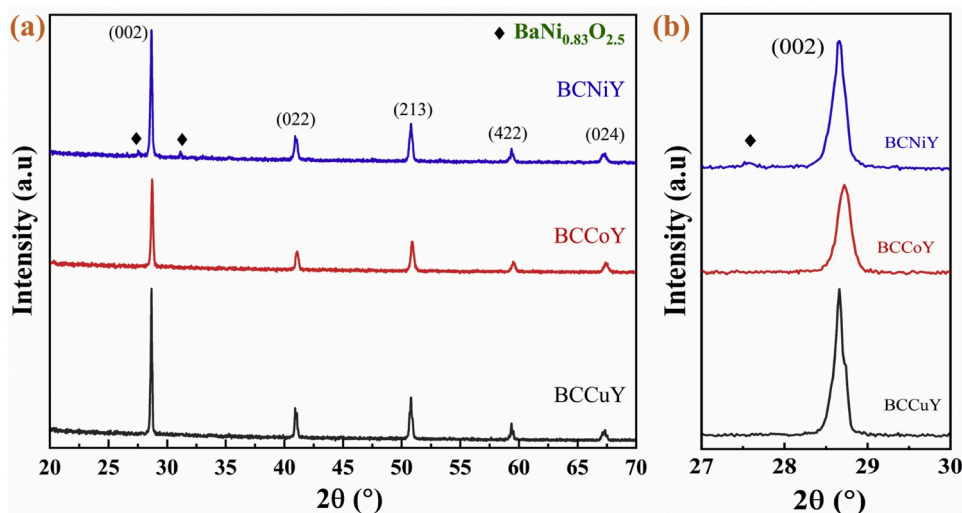


Fig. 2. XRD patterns of BCNiY, BCCoY, and BCCuY are a) synthesized at 1000 °C for 8 h, b) along with the magnified XRD spectra.

analysis was done by suspending them in the acetone via ultrasonication. Eventually, the suspensions were applied carefully onto Au grids painted with holey carbon to ensure even distribution for precise analysis. Fourier transform infrared spectroscopy (FTIR) was performed using IRTracer-100FTIR Spectrometer to examine the functional groups and chemical bonds of BCNiY, BCCoY, and BCCuY cathode materials.

The X-ray Photoelectron Spectroscopy (XPS) studies were performed using a Kratos Axis Ultra DLD photoelectron spectrometer in a multi-chamber Ultrahigh Vacuum (UHV) system coupled with a hemispherical analyzer (SES R4000, Gammatdata Scienta). To generate the core excitation, an X-ray source (non-monochromatized Mg Ka, 1253.6 eV) with an anode operating at 15 mA and 12 kV was employed. The energy resolution of the system operating at a fixed pass energy of 100 eV was 0.9 eV. During the experiment, the pressure in the chamber was about 1×10^{-9} mbar, and the base pressure was about 1×10^{-10} mbar. The analysis area of the sample was about 4 mm². To fix the measured spectra for surface charging the binding energy of the involuntary carbon species was used (C 1 s line at BE = 285.0 eV). CasaXPS software version CasaXPS 2.3.23 was used to fit the obtained data from XPS measurements. Thermogravimetry (TG) and differential scanning calorimetry (DSC) using Thermo Analyzer NETZSCH STA 449 F5 Jupiter was performed in artificial air (50 mL min⁻¹) at a heating rate of 12 °C min⁻¹ to study simultaneously the thermal analysis and stability of BCNiY, BCCoY, and BCCuY cathode materials. For the reference substance, an empty α -Al₂O₃ crucible was used. For the assessments, ca. 12 mg of powdered sample was fired from 35 to 1200 °C in a corundum crucible.

Dynamic light scattering (DLS) technique was performed using a Mastersizer 3000 analyzer to examine the particle size distribution in terms of volume % of BCNiY, BCCoY, and BCCuY powder materials.

For the calculation of crystallite size, the Scherer Eq. (3) is used [37].

$$D = \frac{K\lambda}{\beta \cos\theta} \quad (3)$$

Where $K = 0.94$ Scherer constant, D is crystallite size, θ is Bragg's diffraction angle, and $\lambda = 1.540562$ Å wavelength of X-ray.

2.3. Cell preparation and electrochemical performance

BaCe_{0.875}Mo_{0.025}Y_{0.2}O_{3-δ} (BCM_{0.025}Y) pellets served as electrolytes for electrochemical impedance spectroscopy (EIS) measurements. Whereas BCXY (X = Ni, Co, Cu) cathode powder pastes were screen-printed in a round shape on both sides (symmetric electrodes) of the BCM_{0.025}Y pellets using a screen printer (Aremco 3230). These pastes were carefully mixed with the ink vehicle to obtain the required

rheological properties. After three depositions on each side, the electrodes underwent drying treatment in an oven at 90 °C for 15 min. Subsequently, the cells were sintered in an air furnace at 900 °C for 2 h with a 3 °C/min heating and cooling rate.

The silver paste (FuelCellMaterials) in the form of a mesh pattern was coated using a proper brush on both sides of the electrodes, heated at 750 °C for 30 min, and was used as the current collector. The symmetrical cells were examined to calculate the electrode polarization resistance between 600–750 °C in dry and wet (3 vol. % H₂O) air atmospheres.

The electrochemical performance of the fabricated symmetrical cells was analyzed using the Solartron 1252A frequency response and Solartron SI 1287 electrochemical interface. Impedance spectroscopy was employed in the 0.1 Hz–1 MHz frequency range under open-circuit conditions with a 25 mV of perturbation amplitude. The total interfacial polarizations and ohmic resistance (R_{Ω}) with cathode and anode contributions ($R_p = R_c + R_a$) were refined relative to the $1-R_{\Omega}-(RQ)_{HF}-(RQ)_{LF}$ equivalent circuit, where Q represents - capacitive constant phase element, R - resistance, L - inductance, LF - low-frequency and HF - high-frequency contributions respectively. The Z-view software was used for the EIS fitting.

2.4. Chemical compatibility assessment of BCNiY, BCCoY and BCCuY with typical electrolyte

The BCNiY, BCCoY, and BCCuY cathode materials were assessed for their chemical compatibility with BaCe_{0.6}Zr_{0.2}Y_{0.2}O_{3-δ} (BCZY, Fuel Cell Materials) proton conducting electrolyte. In the assessment, the BCNiY, BCCoY, and BCCuY cathode materials were mixed with BCZY electrolyte powder in a 1:1 wt ratio and ground with the help of a mortar and pestle for about 15 min to obtain a fine powder. After the proper mixing, the powders were annealed in an air furnace at 800 °C for 100 h. At last, the XRD studies were performed on the annealed powders at room temperature.

3. Results and discussion

3.1. Crystal structure properties of BaCe_{0.8}X_{0.1}Y_{0.1}O_{3-δ} compounds

The XRD pattern depicted in Fig. 2a illustrates the combined pattern of BCNiY, BCCoY, and BCCuY cathode material powders, showcasing prominent reflection peaks corresponding to BaCe_{0.8}Y_{0.2}O_{3-δ} (BCY), such as (002), (022), (213), (422), and (024). These peaks confirm the orthorhombic symmetry and perovskite phase of BCY, consistent with

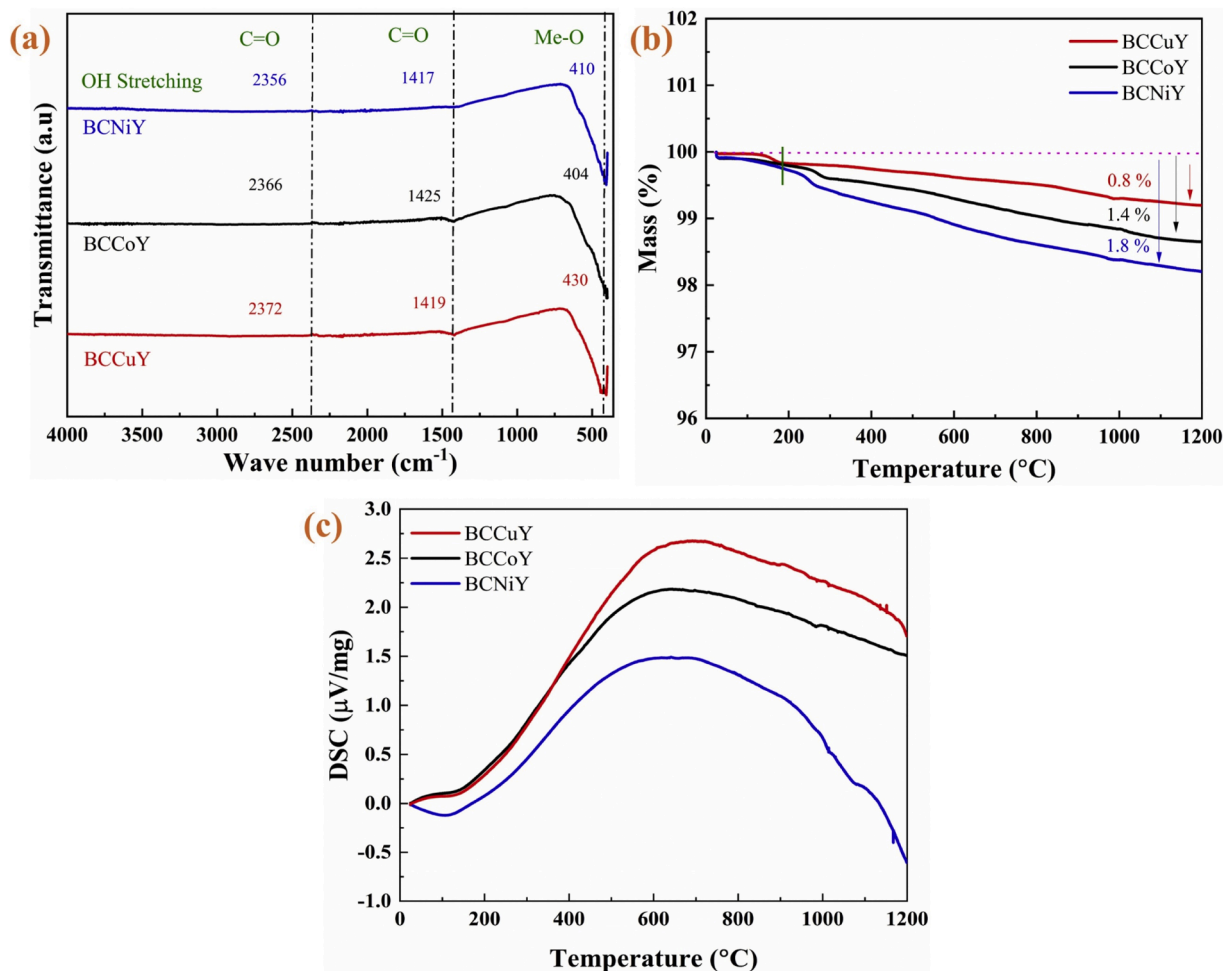


Fig. 3. a) Fourier Transform Infrared Spectroscopy (FTIR) spectra of BCNiY, BCCoY, and BCCuY calcined at 1000 °C for 8 h, b) mass change, and c) DSC measurements for BCNiY (Blue curve), BCCoY (Black curve) and BCCuY (Red curve) compounds in air.

the JCPDS-82-2425 reference. The XRD patterns of BCCoY and BCCuY exhibit pure phase perovskite, while the BCNiY pattern reveals small impurity peaks attributed to the BaNi_{0.83}O_{2.5} phase of rhombohedral symmetry, as indicated by JCPDS-01-082-1913. Such impurity phases are commonly encountered during the synthesis of BCY materials containing Ni, reported in studies utilizing combustion nitrate-based [38, 39] and solid-state routes [40].

Notably, Tong et al. [40] extensively investigated the formation of such impurities in Ni-based BZY materials, suggesting their occurrence at temperatures exceeding 900 °C, persisting even at temperatures up to 1500 °C. These impurities have been associated with increased grain growth and density in BZY materials [40], albeit later studies revealed impediments to proton conductivity, resulting in elevated activation energy for conduction [41,42]. Despite the presence of Cu, Co, and Ni dopants in the materials, their metallic peaks are not observable in the XRD pattern, which indicates that Cu, Co, and Ni cations have been successfully incorporated into the BCY perovskite structure. This means the Cu, Co, and Ni atoms have replaced or occupied positions within the BCY lattice rather than forming a separate or secondary phase. The average crystallite sizes determined using Scherer's Eq. (1) are calculated to be 54.52 nm, 51.26 nm, and 63.88 nm for BCNiY, BCCoY, and BCCuY, respectively. The magnified XRD spectrum of the (002) peak is shown in (Fig. 2b). Shifting of the Peak in XRD directly reflects the change in the crystal structure due to the difference in ionic radii. When larger cations replace smaller cations in the lattice, the unit cell expands, the interplanar spacing (*d*) increasing. According to Bragg's law, this results in a shift to lower angles (*θ*). Conversely, when smaller cations

replace larger cations, the unit cell contracts, decreasing the *d* spacing, causing the shift to higher angles. Peak shifting in the magnified diffraction peak (002) is due to the modified lattice parameters caused by the difference between the ionic radii of the doped metal cations (Ni (Ni²⁺ = 0.69 Å), Cu (Cu²⁺ = 0.73 Å), and Co (Co²⁺ = 0.745 Å and Co³⁺ = 0.61 Å) relative to the other components (Ce, Y) in the B site of perovskite materials (BCY).

3.2. Spectral analysis and thermal stability of BaCe_{0.8}X_{0.1}Y_{0.1}O_{3-δ} materials

Fig. 3a displays the FTIR spectroscopy spectra of BCNiY, BCCoY, and BCCuY cathode materials, heated at 1000 °C for 8 h, in the 400–4000 cm⁻¹ range. All three cathode materials show similar spectra. A weak, broad peak at 3600–3300 cm⁻¹ is related to the O–H stretching vibration due to the presence of OH groups and water adsorption on the surface of barium cerate. The formation of proton defects is associated with the filling of oxygen vacancies by the OH group resulting in enhancing proton conductivity [43].

The stretching vibration observed at ~415 cm⁻¹ is assigned to MO₆ (metal octahedral oxygen). Prominent spectral peaks at positions 410, 404, and 430 cm⁻¹ for BCNiY, BCCoY, and BCCuY, respectively, correspond to the stretching vibration modes correlated with the bridging bond M–O–M, indicating structural distortion due to differences in the size of Ni, Cu, and Co. The successful doping of transition metal-ions into the host material is confirmed by the substantially intense observed peaks in the case of BCCuY, aligning with the XRD results [44].

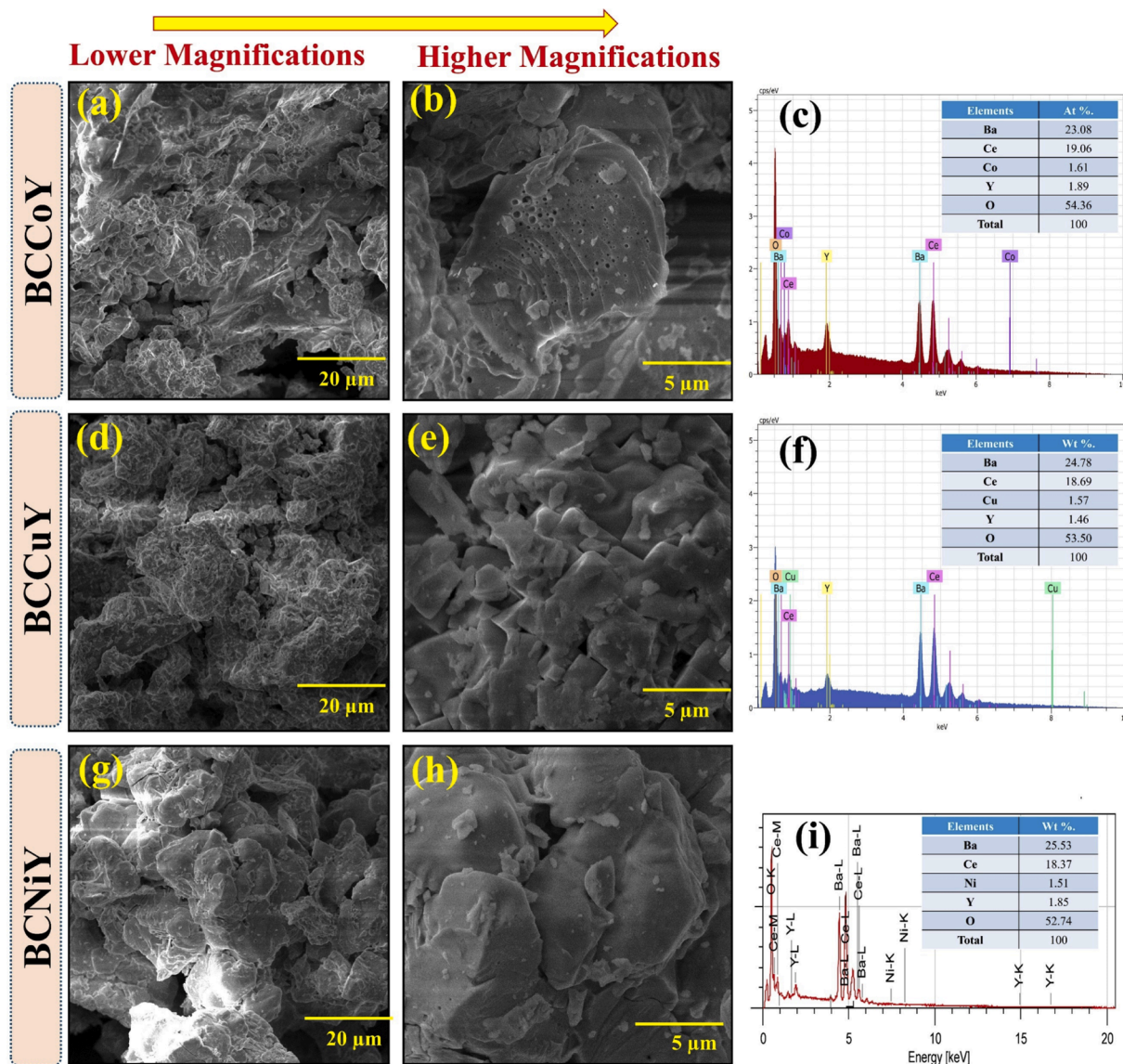


Fig. 4. Surface morphologies from lower to higher magnifications along with the EDS spectra of a-c) BCCoY, d-f) BCCuY, g-i) BCNiY cathode powders.

Weak bands in the range of 1415–1430 cm^{-1} can be assigned to the C–O_{str} vibrations of CO₃²⁻ species (present in the system) and asymmetric and bending stretching [43].

The oxygen content change and thermal stability of BCNiY, BCCoY, and BCCuY cathode materials powders were analyzed through different thermogravimetric analysis (TGA) (Fig. 3b) and differential scanning calorimetry (DSC) (Fig. 3c) in the temperature range 25–1200 °C in an air atmosphere. The observed mass loss in the 25–200 °C range is attributed to water evaporation absorbed on the powders' surface, while the mass loss in the 200–700 °C temperature range is due to the creation of some oxygen vacancies in the cathode materials and dehydration of the perovskite lattices.

The total mass loss for BCNiY, BCCoY, and BCCuY was 1.8 %, 1.4 %, and 0.8 %, respectively. The higher mass loss in BCNiY compared to BCCoY and BCCuY was observed, possibly due to the amount of generated oxygen vacancies and the additional impurities as explained in XRD (Fig. 2). Overall, all three cathode materials present remarkable chemical stability. DSC measurements supported the TGA results depicted in Fig. 3c. No exothermic and endothermic peaks were observed in the DSC graph, which indicates that there is no phase transition. The endothermic and exothermic peaks in the DSC graph indicate phase transitions, where heat is released or absorbed by the material. Therefore, the

absence of such peaks suggests that no phase transitions occur within the tested temperature range, and during the experiment, the materials remain in a stable phase.

3.3. Surface topography and elemental analysis of BCNiY, BCCoY and BCCuY cathodes

Fig. 4 depicts the surface morphology of BCCoY (Figs. 4a and b), BCCuY (Figs. 4d and e), and BCNiY (Figs. 4g and h) powders, providing a comprehensive view from lower to higher magnifications. The SEM images highlight the porous nature of these cathode materials, a characteristic that can significantly enhance catalytic activities by providing more active sites for reactions. Throughout the images, particles are observed to be distributed relatively uniformly across all structures, indicating a well-connected network that can enhance electrochemical performance and conductivity [45]. Notably, BCCuY appears to have smaller particles with less agglomeration compared to BCCoY and BCNiY at similar magnification. This suggests an optimized microstructure, which is essential for achieving high-performance cathode materials for PCFCs. The Dynamic light scattering (DLS) technique was performed to examine the particle size distribution in terms of volume % of BCNiY, BCCoY, and BCCuY powder materials, and the obtained

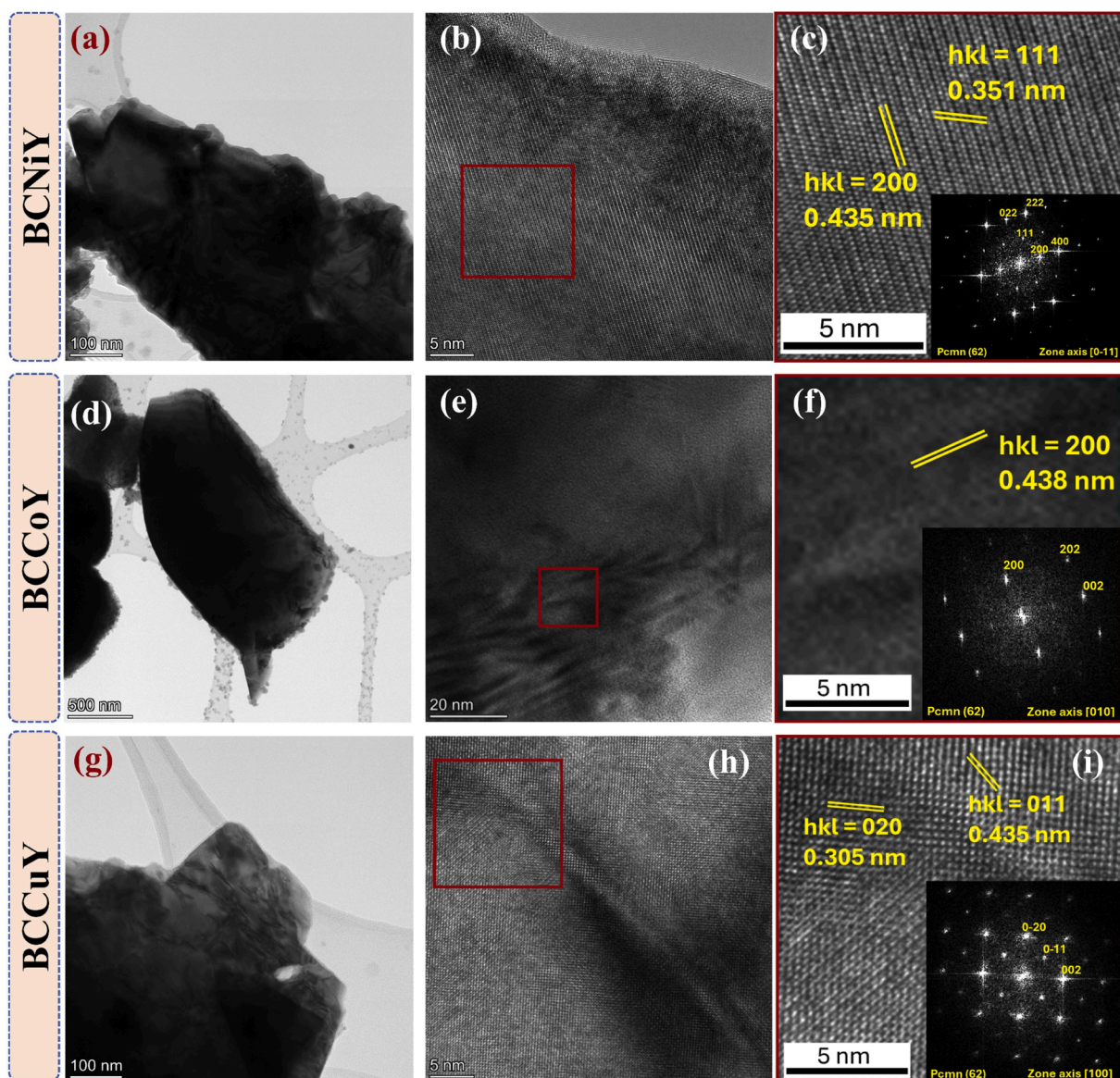


Fig. 5. TEM images a, d, g) of the powder samples of BCNiY, BCCoY, and BCCuY cathodes respectively, b, e, h) HR-TEM images measured for ground powder, and c, f, i) the zoomed region with the inset showing the corresponding FFT pattern with indexed spots assigned to the perovskite structure.

results are shown in the supplementary file **Fig. S3**. The DLS results show that the BCCuY sample has a more significant smaller particle size contribution than BCCoY and BCNiY.

Furthermore, the SEM images also reveal differences in material densification among the three cathode materials. While BCNiY exhibits the most densified structure along with the particle agglomeration which may lead to a decrease in the electrochemical performance. Conversely, BCCoY shows an intermediate level of densification. These variations in microstructure underscore the importance of carefully optimizing synthesis parameters to achieve desired material characteristics and performance outcomes. In addition to SEM analysis, the elemental analysis of the powder materials was measured using Energy-dispersive X-ray Spectroscopy (EDS). The EDS spectra (**Figs. 4c, f, and i**) confirm the presence of all elements expected based on the chemical formula, providing further validation of the synthesis process. The peaks in the spectra correspond to the elements listed in the formula, indicating successful synthesis and adherence to the intended composition.

Figs. 5a, d, and g show the transmission electron microscopy (TEM) images of the powder samples of BCNiY, BCCoY, and BCCuY materials. The Fast Fourier Transform (FFT) was performed on the indicated areas

of the TEM images. The spots in the FFT images correspond to the interplanar distances present in these indicated areas. The measurements of these distances allowed phase confirmation and determination of the particle's orientation. The distances between the lattice fringes are shown in the zoomed region from HR-TEM images. The diffraction spots in BCNiY correspond to the lattice spacing of 3.51 Å and 4.35 Å which could be indexed to (111) and (200) miller planes. In BCCoY the diffraction spots correspond to the lattice spacing of 4.38 Å which could be indexed to (200) miller plane and the diffraction spots in BCCuY correspond to the lattice spacing of 4.35 Å and 3.05 Å which could be indexed to (011) and (020) Miller planes. The high-resolution images of BCNiY, BCCoY, and BCCuY shown in **Fig. 5b, e, and h** directly reveal these lattice planes, respectively.

The presence of the perovskite-type structure is proven by the HR-TEM, with all the observed spots in the FFT pattern assigned to the Pcmn space group (**Fig. 5c-i**).

Figs. 6a-f show the TEM-EDS mapping of the powder samples of a, b) BCNiY, c, d) BCCoY, and e, f) BCCuY cathode materials. The dopant materials are uniformly dispersed in the corresponding crystal structure, showing the successful incorporation of dopant elements into the crystal

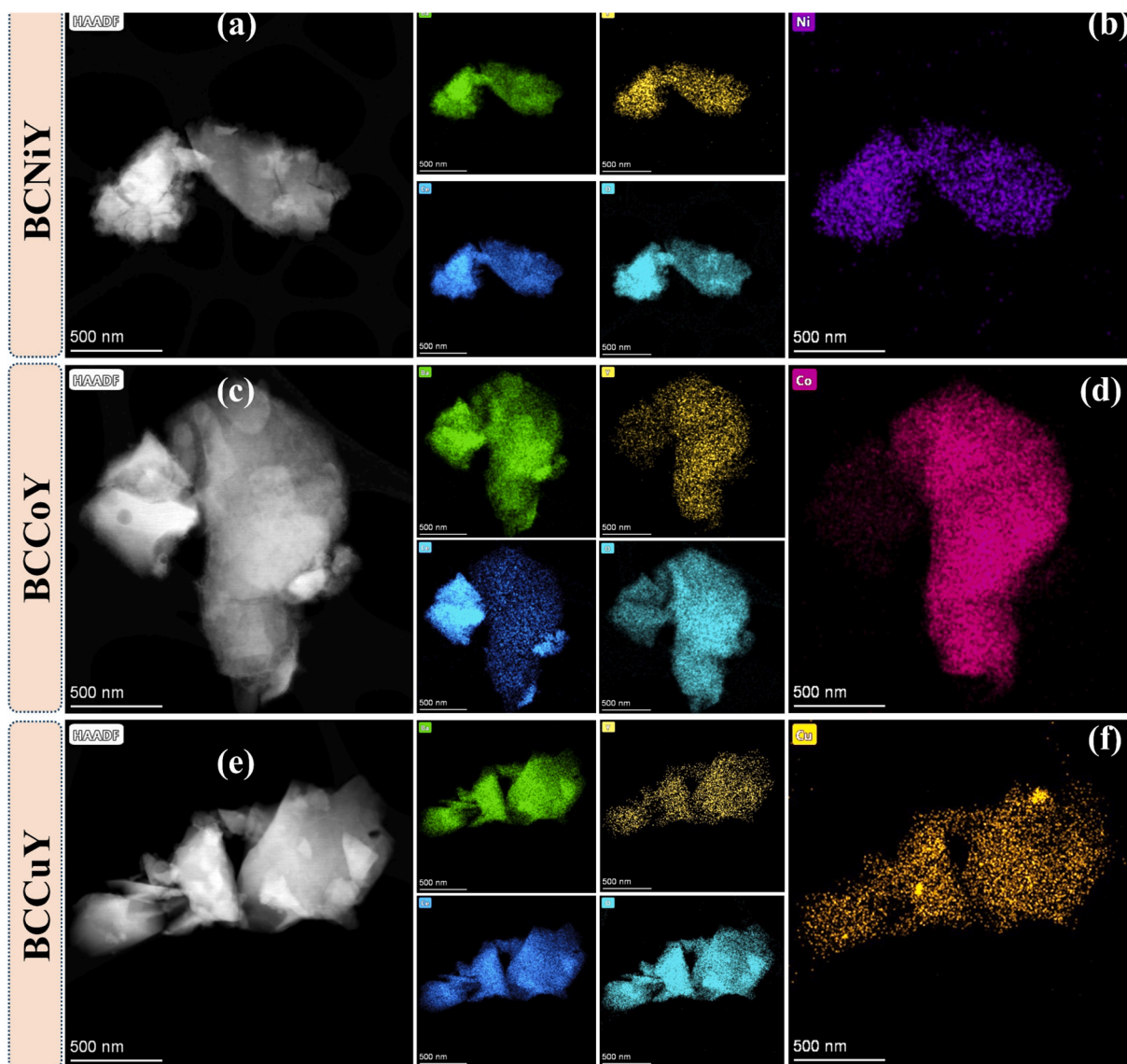


Fig. 6. TEM-EDS mapping of the powder samples: a-b) BCNiY, c-d) BCCoY, and e-f) BCCuY cathodes.

lattice. The synthesized materials are well prepared without any clustering or segregation of the dopant materials in the parent structure. This indicates that no secondary phase was present in the as-prepared single-phase BCY, as confirmed by XRD results (Fig. 2). As confirmed by the EDS spectra, the absence of impurities suggests that the synthesis and doping processes were well-controlled, free from contamination, and ensuring high material purity which is essential for high electrochemical performance.

3.4. Valence state analysis of transition metals in BCNiY, BCCoY, and BCCuY compounds

The XPS studies give information about the chemical bonding, oxidation state, and chemical composition of the individual elements. Figs. 7a, d, and g show the XPS full spectra of BCNiY, BCCoY, and BCCuY, respectively. Ni 2p spectrum was resolved in two characteristic Ni 2p_{1/2} and Ni 2p_{3/2} peaks, located at 851.18 eV and 859.74 eV, respectively, as shown in Fig. 7b. These peaks could be related to the Ni²⁺ oxidation state which may exist in the form of Ni(OH)₂ or NiO [46]. In Fig. 7e, the Co 2p_{1/2} and Co 2p_{3/2} core level spectra are deconvoluted to peaks at a binding energy of 794.55 eV and 779.15 eV for Co³⁺, which are accordant with those studied in the literature [47]. The splitting of

the spin-orbital between the 2p_{1/2} and Co 2p_{3/2} peaks is 15.8 eV, showing the coexistence of the Co²⁺ and Co³⁺ species [47]. Nevertheless, it should be noted that this does not exclude the occurrence of Co²⁺, as the peaks for Co²⁺ are commonly appraised to overlap with the peaks for Ba²⁺ and Co³⁺ [48]. Therefore, it is very difficult to fit the Co 2p peaks to determine quantitatively the surface of Co valence. Besides this, it can be concluded that Co³⁺ could be the main valence state which is consistent with the reported literature data [49].

Fig. 7h shows the XPS core level spectra of Cu 2p at 2p_{1/2} and 2p_{3/2} of the BCCuY cathode material. The first peak corresponds to Cu (0) or metallic copper which can be assigned to the presence of a surface CuO, and this could be due to the exposure of the sample to air. However, the binding energies (BE) of the Cu²⁺ and Cu⁺ for the Cu 2p_{3/2} peaks are 934.31 eV and 932.81 eV, respectively. The satellite peak at around 941.80 eV can be assigned to the Cu²⁺ species [50,51]. Interestingly, no spin-state transitions in Cu⁺/Cu²⁺ cations exist, demonstrating the absence of spin-state transition of Cu⁺/Cu²⁺, which contributes to the decrease in the thermal expansion coefficient of the BCCuY cathode material. The redox cycles of the cathode material are favored by mixed valences.

Considering that the reactive species of oxygen have primarily participated in the oxygen reduction reactions (ORR) on the cathode

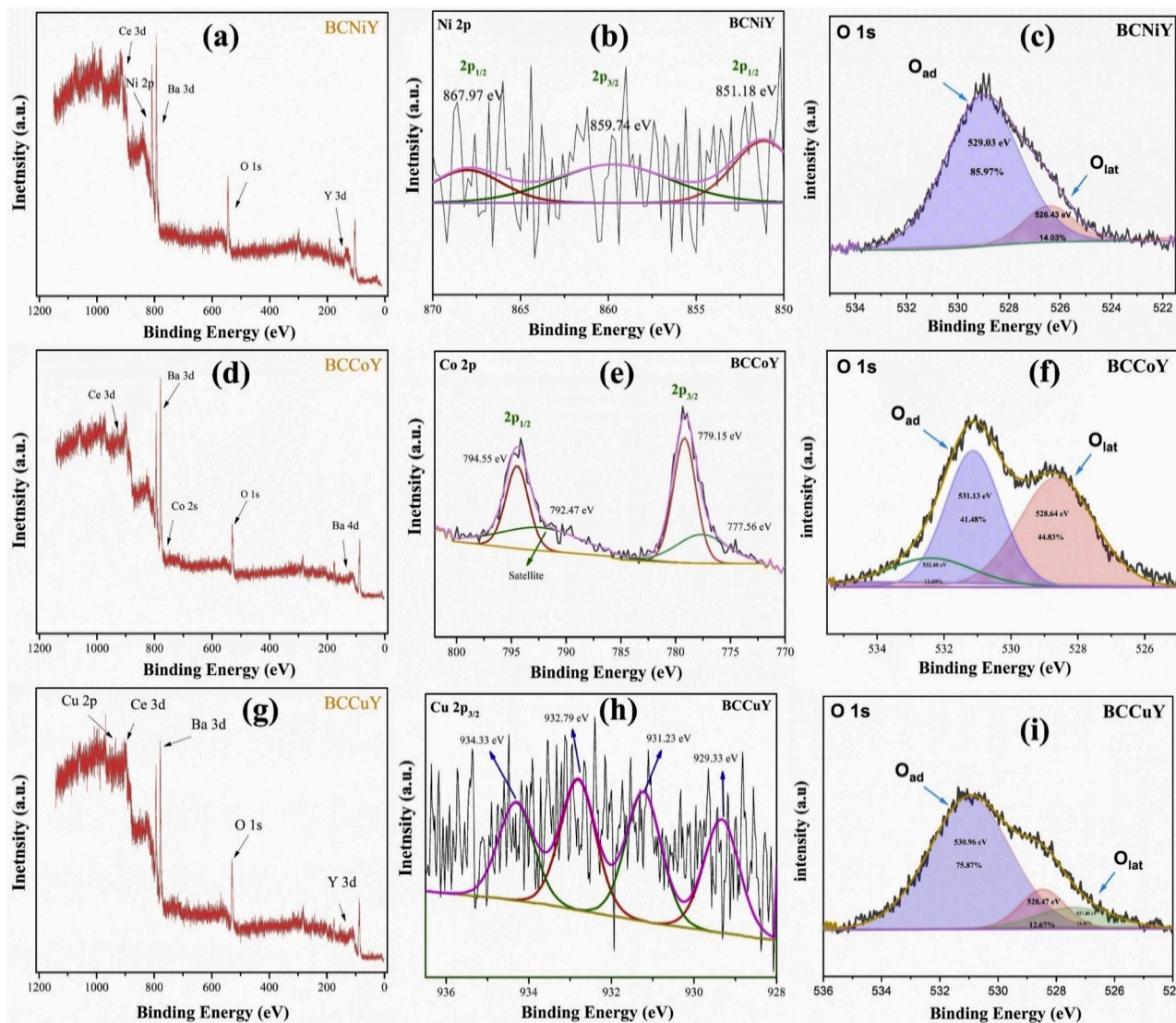


Fig. 7. XPS Spectra of a-c) BCNiY, d-f) BCCoY, and g-i) BCCuY.

side, the response of O 1 s might indicate a combination of different oxygen reaction processes and oxygen-related species (Figs. 7c, f, and i). The peaks at BE of 532.51 eV, 531.14 eV, and 528.51 eV, can correlate with hydroxyl groups ($-\text{OH}$ or CO_3^{2-}) surface adsorbed oxygen ($\text{O}_{2,\text{ad}}$), and lattice oxygen (O^{2-}), respectively [52]. The enhanced electrocatalytic performance in the case of BCCuY cathode material (Fig. 7i) may be ascribed to the enhancement of proton (H^+/OH^-) conduction and oxygen ion transport on the surface of the cathode [53,54]. The O 1 s peak at 532.51 eV might be due to impurities (hydroxyl/carbonyl groups) on the surface of the cathode.

3.5. Electrochemical impedance spectroscopy and activation energy studies

The shape of the graphs obtained from Electrochemical Impedance Spectroscopy (EIS) measurements is temperature-dependent, which could consist of three distinct semicircles in the high-frequency (HF), low-frequency (LF) regions, and medium-frequency (MF), [55,56]. The HF region often corresponds to the intrinsic properties of the bulk material, such as the transport of charge carriers (ions or electrons) through the bulk of the ceramic grains. The MF region often includes contributions from grain boundary resistance (R_{gb}) and the associated capacitance. These grain boundaries can significantly impact the overall

impedance by introducing higher resistance than the bulk material [57]. Meanwhile, in the LF region, impedance is often dominated by electrochemical reactions occurring at the electrode-electrolyte interface, such as charge transfer reactions and mass transport (diffusion) processes [57]. To analyze the impedance spectra, they are fitted using equivalent electrical circuits (EECs). The selected EEC model consists of three subcircuits which are connected in series, each consisting of a parallel combination of a resistor and a constant phase element (CPE). The impedance of a CPE is expressed by the formula:

$$Z_{\text{CPE}_i} = \frac{1}{2\pi f_o C_i} \left(\frac{f_o}{jf} \right)^\alpha \quad (4)$$

whereas,

f = Frequency, f_o = Reference frequency ($f_o = 1000$ Hz), j = Imaginary unit

C_i = Capacitance at the reference frequency, i = Number of pairs of (R, CPE)

α = Coefficient but its values vary between 0.5 and 1, for capacitor, it is 1 and for diffusion, it is 0.5 [58].

The EIS measurements were conducted under dry and wet air

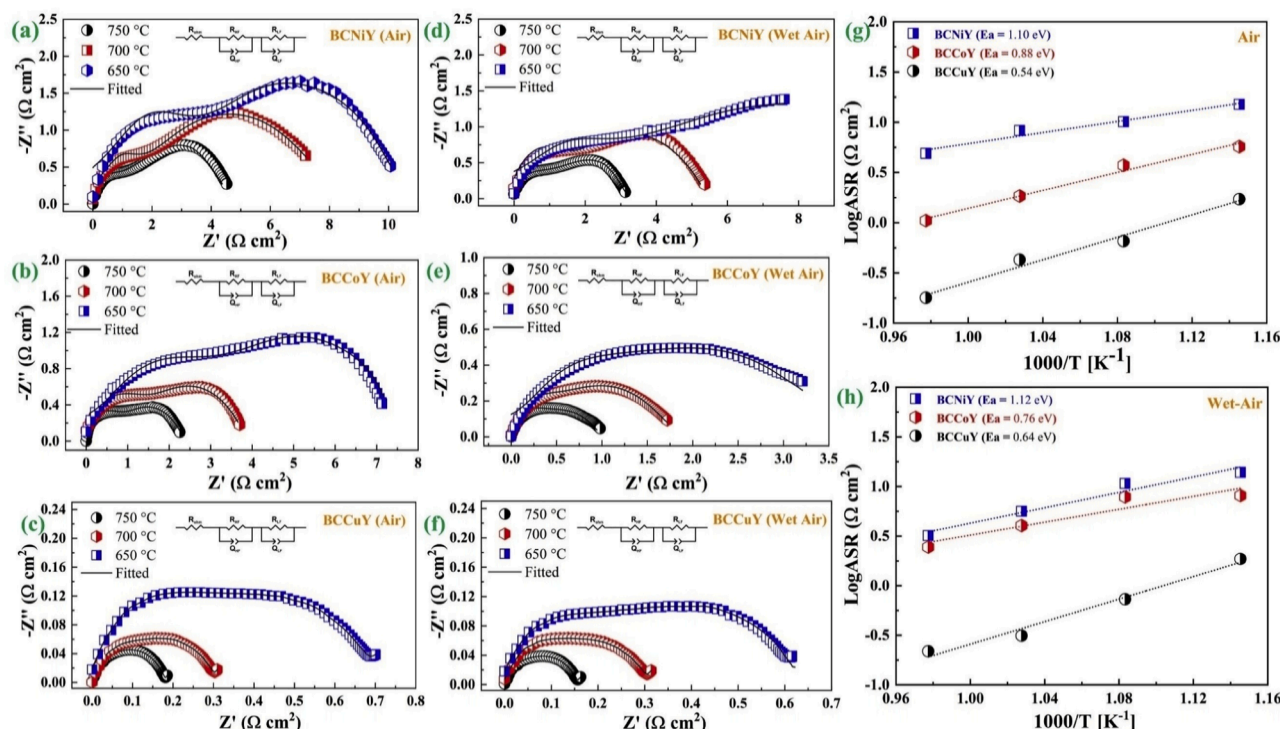


Fig. 8. EIS spectra of BCNiY, BCCoY, and BCCuY cathodes measured from 650 to 750 °C. The spectra are shown for a-c) the dry air atmosphere, and d-f) the wet air atmosphere. Additionally, the Arrhenius plot representing the activation energy is presented for g) dry air atmosphere, and h) wet air atmosphere.

atmospheres, with temperatures, ranging from 600 to 750 °C. Wet air refers to "humidified air" with 3 vol. % water at room temperature. The airflow rate was well controlled by a mass flow meter (controller). **Figs. 8a-c** display the experimental and fitted EIS data for BCNiY, BCCoY, and BCCuY electrodes under dry air, while **Figs. 8d-f** present the corresponding data for these electrodes under wet air. The BCNiY, BCCoY, and BCCuY electrodes exhibit good results in both dry and wet air atmospheres at 750 °C. All three electrodes demonstrate low polarization resistance at intermediate temperature, with lower area-specific resistance (ASR) values observed under wet air conditions compared to dry air, indicating the presence of proton conductivity in the

investigated cathodes. Among them, the BCCuY electrode shows the lowest polarization resistance in both environments. The ASR values of the BCNiY, BCCoY, and BCCuY electrodes at 750 °C under dry air are 4.89, 2.45, and 0.20 $\Omega\cdot\text{cm}^2$, respectively. In the wet air condition, those values are reduced to 3.19, 1.04, and 0.17 $\Omega\cdot\text{cm}^2$, respectively, at the same temperature. In the wet air atmosphere, the presence of water vapor leads to the formation of a hydrated layer on the electrolyte and electrode surfaces. The formed hydrated layer facilitates the movement of ions especially protonic ions, by providing pathways that lower the energy barrier for ion transport. Also, the catalytic activity of electrode surfaces increases due to interaction with water molecules resulting in

Table 1

Comparison of ASR values for various proton ceramic symmetrical cathodes at 750 °C temperatures.

Cathode	Abbreviation	Electrolyte	T (°C) / Atmosphere	ASR ($\Omega\cdot\text{cm}^2$)	Ref
BaZr _{0.1} Co _{0.4} Fe _{0.4} Y _{0.1} O _{3-δ} -Sm _{0.2} Ce _{0.8} O ₂	BZCFY-SDC	BZCY	700 (Dry Air)	0.32	[73]
La ₂ NiO _{4+δ} -BaCe _{0.2} Zr _{0.7} Y _{0.1} O _{3-δ}	LN-BCZY	BZCY	700 (Wet Air)	3.70	[74]
Nd _{1.9} Ba _{0.1} NiO _{4+δ}	NBNO.1	BZCYYb	700 (Wet Air)	1.70	[75]
Nd _{1.95} Ba _{0.05} NiO _{4+δ}	NBN	BCZD	750 (Dry Air)	5.00	[76]
La ₂ NiO _{4+δ} -LaNi _{0.6} Fe _{0.4} O _{3-δ}	LNO-LNF	BZCY	700 (Ambient Air)	1.99	[77]
La _{5.5} WO _{11.25-δ} /La _{0.8} Sr _{0.2} MnO _{3+δ}	LSM - LWO	LWO	750 (Wet Air)	1.40	[69]
Sr ₃ Fe _{1.3} Co _{0.2} Mo _{0.5} O _{7-δ}	SCFMO	BZCY	800 (Dry Air)	0.51	[78]
La _{0.5} Sr _{0.5} Fe _{0.9} Mo _{0.1} O _{3-δ}	LSFMO	BZCY	700 (Wet H ₂)	0.23	[79]
Sr ₃ Fe _{1.5} Mo _{0.5} O _{7-δ}	SFMO	BZCY	800 (Dry Air)	0.39	[78]
SrCo _{0.8} Nb _{0.1} Ta _{0.1} O _{3-δ}	SCNT	BZCY	750 (Wet Air)	0.33	[80]
Nd _{1.95} NiO _{4-δ} -BaZr _{0.1} Ce _{0.7} Y _{0.1} Yb _{0.1} O _{3-δ}	NNO-BZCYYbO	BZCY	750 (Wet Air)	0.43	[81]
La _{1.4} Sr _{0.6} Ni _{0.5} Fe _{0.5} O ₄	LSNF-LWO	LWO	750 (Wet Air)	2.00	[82]
La _{5.6} WO _{11.4}					
Sr ₃ Fe _{1.5-x} Co _x Mo _{0.5} O _{7-δ} BZCY	SCFMO-BZCY	BZCY	800 (Dry Air)	0.24	[78]
BaCe _{0.8} Cu _{0.1} Y _{0.1} O _{3-δ}	BCCuY	BCMY	750 (Wet air)	0.17	[This study]
			750 (Dry air)	0.20	
BaCe _{0.8} Co _{0.1} Y _{0.1} O _{3-δ}	BCCoY	BCMY	750 (Wet Air)	1.04	[This study]
			750 (Dry air)	2.45	
BaCe _{0.8} Ni _{0.1} Y _{0.1} O _{3-δ}	BCNiY	BCMY	750 (Wet Air)	3.19	[This study]
			750 (Dry air)	4.89	

Notes: where BZCYYb = BaZr_{0.1}Ce_{0.7}Y_{0.1}Yb_{0.1}O_{3-δ}, LWO = La_{5.5}WO_{11.25-δ}, BZCY = BaZr_{0.1}Ce_{0.7}Y_{0.2}O_{3-δ}, BCZD = BaCe_{0.5}Zr_{0.3}Dy_{0.2}O_{3-δ}, BCZD = BaCe_{0.5}Zr_{0.3}Dy_{0.2}O_{3-δ} and BCMY = BaCe_{0.875}Mo_{0.025}Y_{0.2}O_{3-δ}.

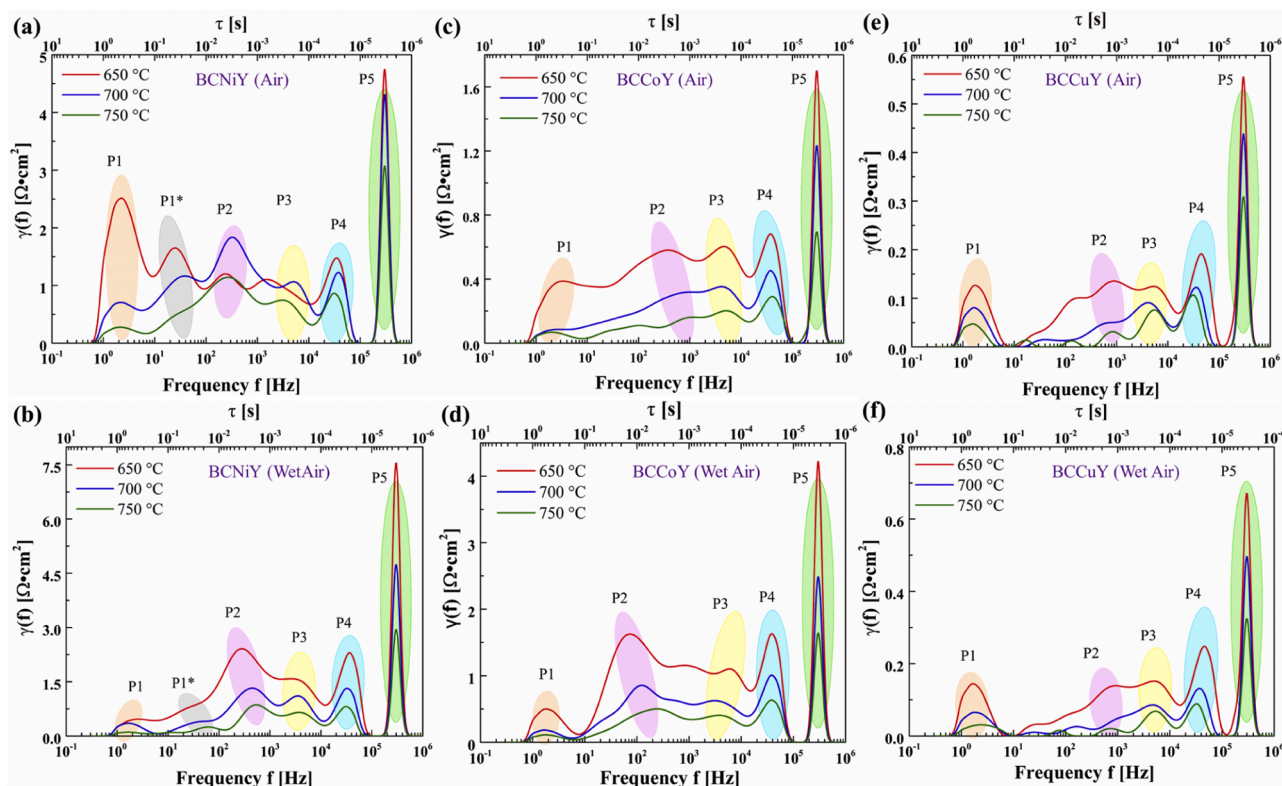


Fig. 9. Distribution of Relaxation Times (DRT) analysis of a-b) BCNiY, c-d) BCCoY, and d-e) BCCuY in dry and wet atmospheres.

faster electrochemical reactions and lower polarization resistance. The lowest polarization resistance recorded for BCCuY might be due to some factors like Cu enhancing the catalytic activity for oxygen reduction reactions, improving ionic and electronic conductivities, and contributing to the formation of stable and compatible phases with BCY. Additionally, from the SEM study, we observed more uniform and finer grain structures of BCCuY, which increase the active surface area for electrochemical reactions and facilitate better mass transport. The equivalent circuit used for fitting in ZView software is shown in the inset of each EIS graph (Fig. 8a-f).

Figs. 8 g and h show the Arrhenius plots representing the activation energy for the BCNiY, BCCoY, and BCCuY cathodes under dry and wet air atmospheres. The calculated activation energies for BCNiY, BCCoY, and BCCuY in dry air are 1.10 eV, 0.88 eV, and 0.54 eV, respectively. Under wet air, these values are 1.12 eV (BCNiY), 0.76 eV (BCCoY), and 0.64 eV (BCCuY), respectively. Under dry air, the activation energies for BCNiY, BCCoY, and BCCuY are relatively lower compared to those measured in wet air. In dry air, the predominant conduction mechanism is typically oxygen ion conduction. The lower activation energies in this condition suggest that the oxygen ions' movement through the electrolyte encounters fewer barriers, leading to more efficient conduction. In contrast, under wet air conditions, the presence of water vapor introduces protonic conduction. Protons have different transport properties compared to oxygen ions, often encountering higher activation barriers due to interaction with the lattice and defect sites. This results in higher activation energies for the same materials under wet air conditions [59,60]. In the case of BCCoY, the lower activation energy in wet air may be due to the efficient hydration process. The cobalt doping in BCY might improve the ability of the material to integrate water into the crystal lattice, resulting in increasing the concentration of proton defect which facilitates the movement of proton ions [61,62].

The ASR values of relevant reported studies of different symmetrical electrodes with different electrolytes at 750 °C are compared with the cathodes of the present study in Table. S1, and symmetrical electrodes with

proton conducting electrolyte (see Table 1) to illustrate the importance of this study. If the literature data is not available at 750 °C, then the corresponding measurement temperature is included. BCCuY exhibited lower ASR values of 0.20 $\Omega\cdot\text{cm}^2$ compared to $(\text{La}_{0.65}\text{Bi}_{0.1}\text{Sr}_{0.25}\text{Cr}_{0.5}\text{Fe}_{0.5}\text{O}_{3-\delta}\text{Sm}_{0.2}\text{Ce}_{0.8}\text{O}_{1.9})$ [63], $\text{La}_{0.8}\text{Sr}_{0.2}\text{MnO}_{3-\delta}\text{Gd}_{0.2}\text{Ce}_{0.8}\text{O}_{2-\delta}$ (LSM-GDC) [64], $(\text{La}_{0.8}\text{Sr}_{0.2}\text{FeO}_{3-\delta})$ [65], $(\text{CaFe}_{0.4}\text{Ti}_{0.6}\text{O}_{3-\delta})$ [66], $(\text{La}_{0.8}\text{Sr}_{1.2}\text{FeO}_4)$ [67], whose ASR values are 4 $\Omega\cdot\text{cm}^2$ and 0.37 $\Omega\cdot\text{cm}^2$, 0.31 $\Omega\cdot\text{cm}^2$, 1 $\Omega\cdot\text{cm}^2$ and 0.43 $\Omega\cdot\text{cm}^2$ in dry air atmosphere, respectively. Under wet air and a wet H_2 atmosphere the symmetrical cathodes such as $\text{SbBaMn}_2\text{O}_{5+\delta}$ (SBM) [68], $\text{La}_{5.5}\text{WO}_{11.25-\delta}\text{La}_{0.8}\text{Sr}_{0.2}\text{MnO}_{3+\delta}$ (LWO-LSM) [69], $(\text{La}_{0.8}\text{Sr}_{0.2})_{0.9}\text{Sc}_{0.2}\text{Mn}_{0.8}\text{O}_{3-\delta}$ (LSSM) [70] $\text{Ca}_3\text{Co}_4\text{O}_9$ (C349) [71], $\text{Ca}_3\text{Co}_4\text{O}_{9-\delta} + \text{PrO}_x$ (C349 – PrO_x) [71], and $\text{Ca}_3\text{Co}_4\text{O}_{9-\delta}$ [72], also have higher ASR values which are 4.16, 1.40, 3.5, and 25.0 $\Omega\cdot\text{cm}^2$, respectively, compared to our synthesized BCCuY cathode as shown in Table. S1. In this study, the ASR value of BCCuY is the lowest, with BCCoY and BCNiY also showing competitive values compared to the literature in both dry and wet air atmospheres. Compared to symmetrical electrodes with proton-conducting electrolytes, the BCCuY also exhibited lower ASR values in dry and wet air atmospheres as shown in Table 1. Additionally, the comparison study of the R_p values of BCNiY, BCCoY, and BCCuY cathodes at 750 °C in dry and wet air atmospheres is plotted in Figures S1a and b (in Supplementary data). The comparison EIS plots at 750 °C clearly show that the BCCuY cathode has the lowest R_p values in dry and wet air atmospheres compared to BCNiY, and BCCoY cathodes. There are several key factors that are responsible for the low R_p value observed in BCCuY cathode compared to BCNiY and BCCoY cathodes. The presence of Cu in BCCuY may significantly enhance the catalytic activities for ORR reactions, as high catalytic activity in ORR reactions is essential for improving electrochemical performance. The Cu dopant may contribute to improving the electronic conductivity by amending the electronic structure of the BCY perovskite resulting in effectual charge transport which is essential for the ORR process. Also, the oxidation state of Cu alternates between Cu^{2+} and Cu^{1+} (observed in XPS studies) which can help in the reduction of oxygen molecules and further promote the ORR activity. Additionally, Cu supports the formation of stable

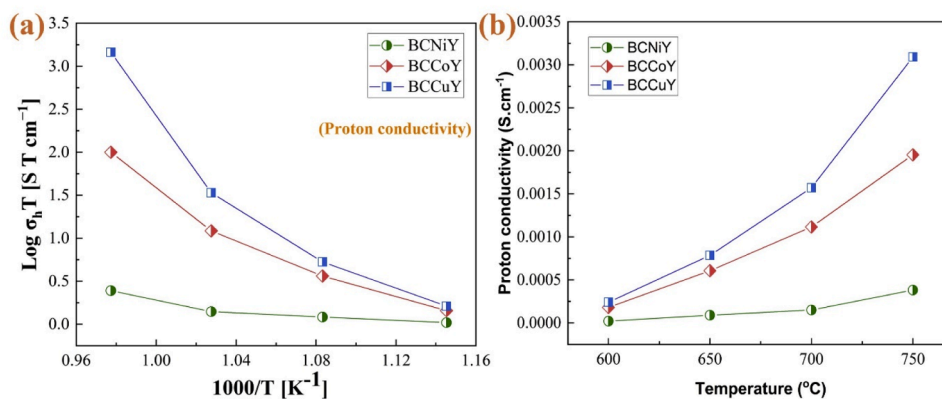


Fig. 10. a) Arrhenius plot represents temperature-dependence proton conductivity and b) Temperature versus proton conductivity plot of BCNiY, BCCoY, and BCCuY cathodes.

and compatible phases with BCY, helping to maintain operational stability and structural integrity. Besides that, BCCuY is more chemically stable compared to BCCoY and BCNiY according to TGA results (Fig. 3b). Cu doping leads to a more refined microstructure of BCY and has a more porous network that can significantly enhance catalytic activities by providing more active sites for ORR reactions [8] as well as smaller particles with less agglomeration compared to BCCoY and BCNiY according to the SEM study (Fig. 4), which is essential for achieving high-performance cathode materials for PCFCs. From the cross-section study of the electrodes, the BCCuY electrode has a smaller particle and grain size with less agglomeration compared to BCCoY and BCNiY electrodes (Fig. 11) which has an impact on the electrochemical performance. The small particle and grain sizes contribute more grain boundaries and larger surface area which improve electrochemical reactions by providing more active sites for reactions and pathways for ion migration that result in lower polarization resistance and enhance the overall performance. All these factors as discussed above together contribute to decreasing the R_p values and increasing conductivity. Therefore, it is concluded that BCCuY is a prominent cathode material for PCFCs.

The Distribution of Relaxation Times (DRT) analysis of EIS measurements was conducted to gain a deeper insight into polarization processes, as shown in Figs. 9a-f, at a temperature from 650 to 750 °C range. The DRT curve is divided into three spectral regions corresponding to high ($\sim 10^5$ – 10^6 Hz), medium ($\sim 10^5$ – 10^2 Hz), and low frequencies (10^2 – 10^{-1} Hz). Each peak represents a specific sub-process, with the peak area reflecting the resistance of that process. The low-frequency response corresponds to oxygen diffusion and adsorption, while the medium and high-frequency responses are associated with charge transfer and oxygen ion migration. Five DRT peaks, ranging from low to high frequency, are labeled P1 to P5. The intensities of the peaks P1 to P5 decrease as the operating temperature increases due to the higher reaction rate at high temperatures. In some cases, the peaks P1 to P3 shift to lower frequencies, while peaks P4 and P5 shift to higher frequencies. According to relevant research literature [83–85], the P1 to P5 peaks may correspond to specific reaction steps. P5 may show the diffusion process of protons to the electrolyte and their incorporation into the electrode lattice. P4 and P3 may show the processes of dissociation, H_2 adsorption, and formation of protons at the electrode. P3 and P2 are typically associated with the cathodic reaction, including the dissociation and adsorption of O_2 on the surface of the cathode, O_2 reduction, and O_2 diffusion to the boundary, and P1 is commonly related to the electrode porous structure for BCNiY, BCCoY, and BCCuY. Additionally, one peak between P2 and P1, represented as Padd was detected in the low-temperature section, which might be attributed to the oxygen reduction process ($O^- \rightarrow O^{2-}$). The oxygen reduction reaction, linked to Padd, is the slowest step in the electrode reaction at low temperatures, limiting the overall performance of the cell. The DRT results are

consistent with the EIS spectra, where higher polarization resistance was observed for BCCoY and BCNiY.

3.6. Electrical and proton conductivities of BCNiY, BCCoY and BCCuY

From the EIS data, the electrical and temperature-dependent electrical conductivities of BCNiY, BCCoY, and BCCuY cathodes in dry and wet air atmospheres were calculated, as shown in the supplementary file **Figure S2a-d** using Arrhenius type plots. The calculated electrical conductivity values in both dry and wet air atmospheres are summarised in **Table S2**. **Figures S2a and b** show the temperature-dependence electrical conductivity, representing Arrhenius-type plots, of BCNiY, BCCoY, and BCCuY cathodes in dry air and wet air atmospheres, respectively. From the figures, it is observed that the BCNiY, BCCoY, and BCCuY cathodes have high electrical conductivity in wet air and low electrical conductivity in dry air atmospheres. In a wet-air atmosphere, the BCNiY, BCCoY, and BCCuY cathodes have higher conductivity than in a dry-air atmosphere due to several phenomena. In a wet atmosphere, the presence of water facilitates the movement of ions (proton and oxygen) by creating oxygen and proton vacancies resulting in enhancing ionic mobility. Additionally, the presence of water vapor prevents the formation of the oxide layer on the surface of the cathode resulting in better conductivity. Such effect is limited in dry air atmosphere resulting in lower conductivity. In conclusion, the higher conductivity in wet air atmosphere is due to the water vapor which facilitates both electronic and ionic conductivities. In comparison to BCNiY and BCCoY cathodes, the BCCuY cathode has a higher conductivity in both dry and wet air atmospheres which is due to lower polarization resistance as discussed.

Figures S3c-d show the temperature versus electrical conductivity of BCNiY, BCCoY, and BCCuY cathodes in dry air and wet air atmospheres, respectively. It is observed from the figure that the electrical conductivity is increasing with increasing temperature. Because at high temperatures the charge carriers are thermally excited which reduces the overall impedance and increases the thermal energy, and such factors enhance the mobility of charge carriers and move freely throughout the material.

The calculated electrical conductivities in both dry and wet air atmospheres allowed to estimate the proton conductivity as well as the proton transference number. The estimation of proton conductivity was done by taking the difference between the electrical conductivity measurements between wet air and dry air atmospheres. The proton transference numbers were estimated by taking the ratio of proton conductivity to the total electrical conductivity measured in the wet air atmosphere. The proton conductivity and proton transference numbers are summarised in **Table S2**. Interestingly, for BCNiY and BCCoY samples, the proton transference number has achieved its highest value at 650 °C. With the increase in temperature (above 650 °C), the possible

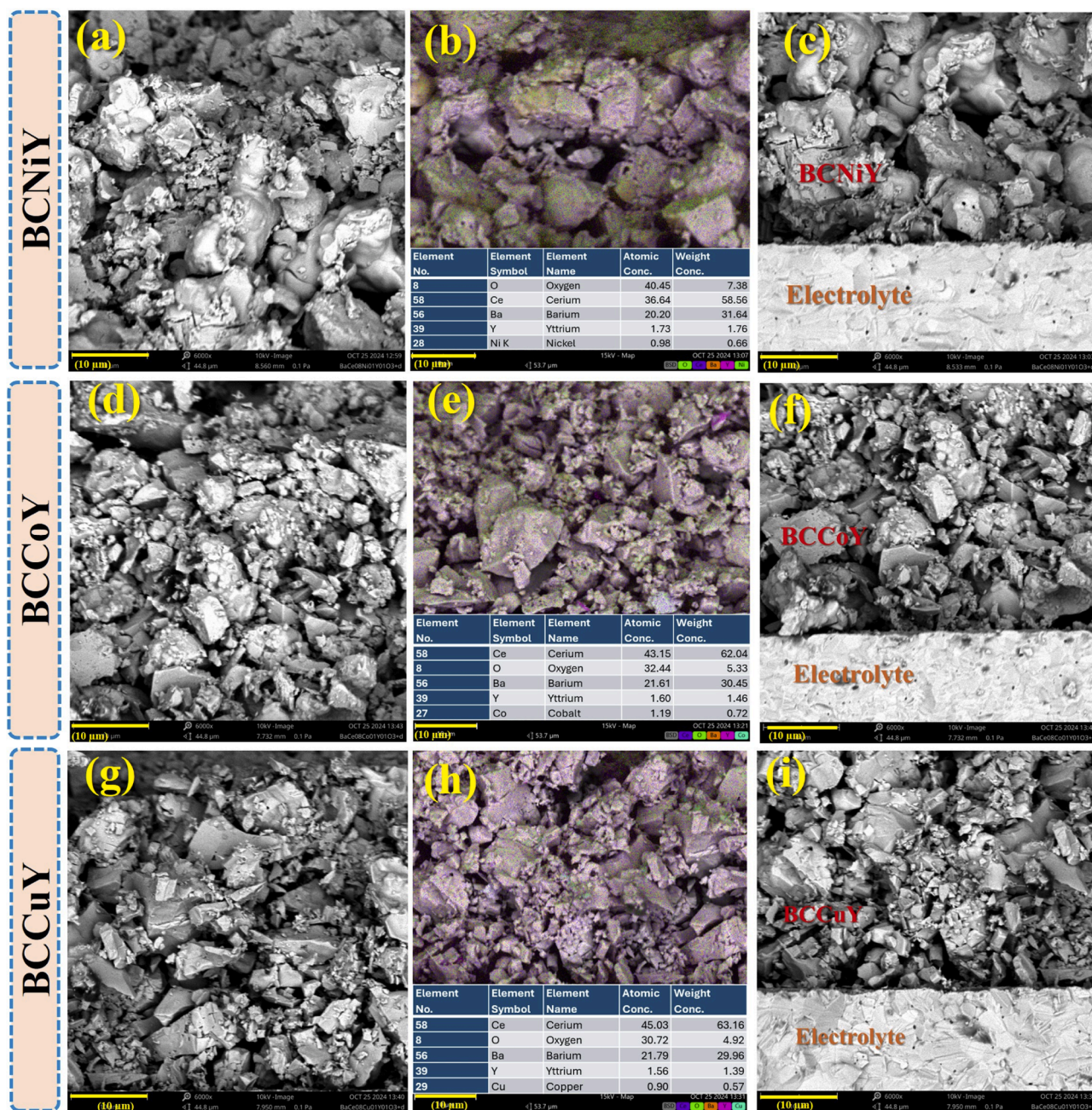


Fig. 11. SEM studies of the surface, EDS mapping, and cross-section of a-c) BCNiY, d-f) BCCoY, and g-i) BCCuY electrodes after the EIS measurements.

appearance of oxygen ionic conductivity in samples decreases the proton transference numbers. In the case of BCCuY, the highest proton transference number is recorded at 600 °C (with a value of 0.29).

Figs. 10a-b show the Arrhenius plot represents temperature-dependence proton conductivity and temperature versus proton conductivity plots of BCNiY, BCCoY, and BCCuY cathodes, respectively. The figures show that BCCuY cathode has high proton conductivity compared to BCCoY and BCNiY cathodes. The high proton conductivity in the case of BCCuY cathode might be due to some factors like Cu enhancing the catalytic activity for oxygen reduction reactions which results in improving both ionic and electronic conductivities and contributing to the formation of stable and compatible phases with BCY perovskite. The proton conductivity increases with increasing temperature because the high temperatures reduce the barriers to the proton moment and increase proton mobility.

3.7. Post-mortem analysis of studied electrodes

Figs. 11a-i show the surface, EDS mapping, and cross-section of the BCNiY (Figs. 11a-c), BCCoY (Figs. 11d-f), and BCCuY (Figs. 11g-i) electrodes after the EIS measurements. The deposition layer thickness of all three symmetrical electrodes is about 35 μm . As we can see the surface and the cross-section of the three electrodes show excellent porosity, and these porosities were maintained during the EIS measurement. No chemical reaction or intermediate layer between the electrodes and the electrolyte is observed after the sintering and EIS testing, and all three electrodes are firmly bonded with the electrolyte. In comparison, the BCCuY electrode has a smaller grain size and particle size and less agglomeration compared to BCCoY and BCNiY electrodes (Figs. 11a-i and Figure S5a-f) which have an impact on the electrochemical performance. The determination of the grain size analysis was

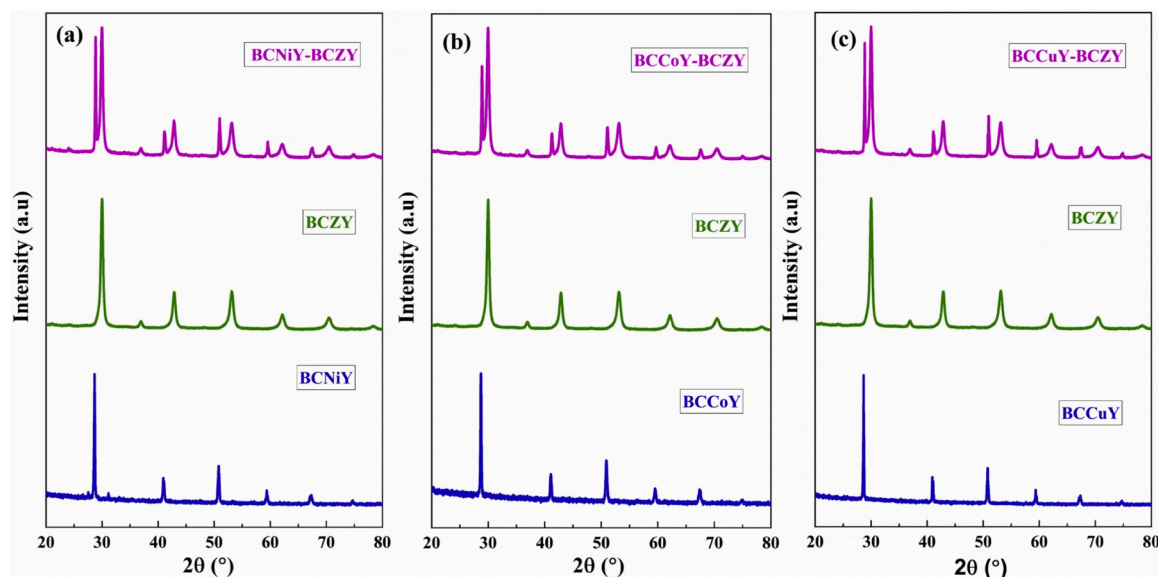


Fig. 12. XRD studies of the annealed powders of a) BCNiY, b) BCCoY, and c) BCCuY cathode materials with BCZY electrolyte.

performed by the line intercept technique using ImageJ software, the obtained results show that BCCuY has a smaller grain size compared to BCCoY and BCNiY cathode materials, supplementary file (Figures S4a-c). Therefore, according to the EIS measurement, the BCCuY electrode has a smaller polarization resistance compared to BCCoY and BCNiY electrodes. The EDS mapping, clearly shows that all three dopants (Ni, Co, and Cu) are uniformly distributed in the corresponding oxides, showing the successful incorporation of dopant elements into the crystal lattice. Overall results show that all three BCNiY, BCCoY, and BCCuY electrodes have good compatibility with the electrolyte.

3.8. Long-term chemical compatibility evaluation with BCZY solid electrolyte

The long-term chemical compatibility evaluation studies of BCNiY, BCCoY, and BCCuY cathode materials with proton conducting BCZY solid electrolyte were conducted for 100 hrs. The chemical compatibility evaluation studies were performed by mixing the BCNiY, BCCoY, and BCCuY powders by a 1:1 wt ratio with BCZY powder and properly mixed it via grinding. The ground powders were annealed in an air furnace at 800 °C for 100 hrs. The XRD measurements of the annealed powders were performed at room temperature. Figs. 12a-c show the XRD patterns of the BCNiY (Figs. 12a), BCCoY (Figs. 12b), and BCCuY (Figs. 12c) powders with BCZY powder after annealed at 800 °C for 100 hrs. No secondary phase or impurities peaks were observed in the XRD pattern after the long-term compatibility studies, showing that BCNiY, BCCoY, and BCCuY cathodes are stable and chemically compatible with BCZY electrolyte.

4. Conclusions

The Ni, Co, and Cu-doped BCY cathode materials for proton-conducting solid oxide fuel cells (PCFCs) were synthesized via the Sol-gel technique, and their microstructural and electrical conductivity properties were systematically investigated. The crystal structure, surface morphology, microstructure, elemental composition, oxidation state, chemical bonding, oxygen content change, and electrode polarization properties of the cathode materials were characterized by XRD, SEM, TEM, EDS, XPS, TGA/DSC, FTIR, and EIS studies, respectively. TGA/DSC study indicated that all three materials possess excellent chemical stability, with BCCuY exhibiting a very low weight loss of 0.8 % compared to BCNiY and BCCoY, which may indicate a rather low

content of oxygen vacancies generated in this oxide, showing the further increase of doping content could be of great interest. The SEM and TEM analysis shows that all the particles are well connected, which results in improving the catalytic activities of materials. The EDS study confirmed the presence of dopants and the corresponding elements with no impurities in all three materials. Preliminary results from electrochemical impedance spectroscopy showed that all three cathodes have low polarization resistance at 750 °C in dry and wet air atmospheres. BCCuY demonstrated the lowest polarization resistance ($0.21 \Omega\text{-cm}^2$ in dry air and $0.17 \Omega\text{-cm}^2$ in wet air) and activation energy (BCCuY: 0.64 eV, BCCoY: 0.76 eV, BCNiY: 1.12 eV). Long-term chemical compatibility evaluation showed that all three electrode materials demonstrated excellent chemical compatibility with BCZY electrolytes. Overall, BCCuY showed superior electrochemical performance compared to BCCoY and BCNiY, featuring its potential as a novel cathode material for PCFCs. This work shows the strategy of doping transition metals in $\text{BaCeO}_{3-\delta}$ -type oxides could be of great interest for the successful development of novel oxygen electrodes for PCFCs. Future research work should focus on increasing the concentration of Cu or co-doping Cu with other transition metals, as this might further enhance catalytic activity in oxygen reduction reactions. Additionally, full fuel cell performance and long-term stability measurements are essential to optimize the applicability in commercial PCFCs.

CRediT authorship contribution statement

Amir Sultan: Writing – review & editing, Writing – original draft, Visualization, Methodology, Investigation, Data curation, Conceptualization. **Michał Gogacz:** Methodology, Investigation. **Jakub Lach:** Methodology, Investigation. **Richard T. Baker:** Methodology, Investigation. **Muhammad Ali Khalid:** Methodology, Investigation. **Yihan Ling:** Writing – review & editing, Methodology. **Kun Zheng:** Writing – review & editing, Visualization, Supervision, Project administration, Methodology, Investigation, Funding acquisition, Data curation, Conceptualization.

Declaration of competing interest

The authors declare that they have no known competing financial interests or personal relationships that could have appeared to influence the work reported in this paper.

Acknowledgment

This work was supported by the research project within the program „Excellence Initiative – Research University” for the AGH University of Krakow. Amir Sultan would like to thank the support from the Polish National Agency for Academic Exchange NAWA under the Programme STER-Internationalization of Doctoral School, Project no BPI/STE/2023/1/00027/U/00001. We would like to express our heartfelt gratitude to the late Prof. Michał Mosiałek for his invaluable contributions to this research. As the previous supervisor of Amir Sultan, he played a pivotal role in shaping this work through his extensive expertise and guidance. We are deeply saddened by his passing, and we include this special acknowledgment to honor his memory and enduring impact on this study.

Supplementary materials

Supplementary material associated with this article can be found, in the online version, at [doi:10.1016/j.electacta.2025.146127](https://doi.org/10.1016/j.electacta.2025.146127).

Data availability

Data will be made available on request.

References

- J. Yu, N. Tian, Y. Deng, G. Li, L. Liu, L. Cheng, K. Qi, Fabrication and characterization of $\text{BaCe}_{0.8}\text{Y}_{0.2}\text{O}_{2.9}\text{-Ce}_{0.85}\text{Sm}_{0.15}\text{O}_{1.925}$ composite electrolytes for IT-SOFCs, *Sci. China Chem.* 58 (2015) 473–477, <https://doi.org/10.1007/s11426-014-5176-x>.
- D. Xu, X. Liu, D. Wang, G. Yi, Y. Gao, D. Zhang, W. Su, Fabrication and characterization of SDC–LSGM composite electrolytes material in IT-SOFCs, *J. Alloys. Compd.* 429 (1–2) (2007) 292–295, <https://doi.org/10.1016/j.jallcom.2006.04.009>.
- B. Butz, P. Kruse, H. Störmer, D. Gerthsen, A. Müller, A. Weber, E. Ivers-Tiffée, Correlation between microstructure and degradation in conductivity for cubic Y_2O_3 -doped ZrO_2 , *Solid. State Ion.* 177 (37–38) (2006) 3275–3284, <https://doi.org/10.1016/j.ssi.2006.09.003>.
- E.D. Wachsman, K.T. Lee, Lowering the temperature of solid oxide fuel cells, *Science* (1979) 334 (6058) (2011) 935–939, <https://doi.org/10.1126/science.1204090>.
- G. Heras-Juaristi, U. Amador, R.O. Fuentes, A.L. Chinelatto, J.R. de Paz, C. Ritter, G.C. Mather, Thermal evolution of structures and conductivity of Pr-substituted $\text{BaZr}_{0.7}\text{Ce}_{0.2}\text{Y}_{0.1}\text{O}_{3-\delta}$: potential cathode components for protonic ceramic fuel cells, *J. Mater. Chem. A* 6 (13) (2018) 5324–5334, <https://doi.org/10.1039/C7TA09570H>.
- L. Yang, S. Wang, K. Blinn, M. Liu, Z. Liu, Z. Cheng, M. Liu, Enhanced sulfur and coking tolerance of a mixed ion conductor for SOFCs: $\text{BaZr}_{0.1}\text{Ce}_{0.7}\text{Y}_{0.2-x}\text{Yb}_x\text{O}_{3-\delta}$, *Science* (1979) 326 (5949) (2009) 126–129, <https://doi.org/10.1126/science.1174811>.
- K. Wei, N. Li, Y. Wu, W. Song, X. Wang, L. Guo, Y. Ling, Characterization and optimization of highly active and Ba-deficient $\text{BaCo}_{0.4}\text{Fe}_{0.4}\text{Zr}_{0.1}\text{Y}_{0.1}\text{O}_{3-\delta}$ -based cathode materials for protonic ceramics fuel cells, *Ceram. Int.* 45 (15) (2019) 18583–18591, <https://doi.org/10.1016/j.ceramint.2019.06.081>.
- Y. Song, Y. Chen, W. Wang, C. Zhou, Y. Zhong, G. Yang, Z. Shao, Self-assembled triple-conducting nanocomposite as a superior protonic ceramic fuel cell cathode, *Joule* 3 (11) (2019) 2842–2853, <https://doi.org/10.1016/j.joule.2019.07.004>.
- Y. Lin, R. Ran, Y. Zheng, Z. Shao, W. Jin, N. Xu, J. Ahn, Evaluation of $\text{Ba}_{0.5}\text{Sr}_{0.5}\text{Co}_{0.8}\text{Fe}_{0.2}\text{O}_{3-\delta}$ as a potential cathode for an anode-supported proton-conducting solid-oxide fuel cell, *J. Power. Sources.* 180 (1) (2008) 15–22, <https://doi.org/10.1016/j.jpowsour.2008.02.044>.
- N. Bonanos, Transport properties and conduction mechanism in high-temperature protonic conductors, *Solid. State Ion.* 53 (1992) 967–974, [https://doi.org/10.1016/0167-2738\(92\)90278-W](https://doi.org/10.1016/0167-2738(92)90278-W).
- K. Xie, R. Yan, X. Chen, S. Wang, Y. Jiang, X. Liu, G. Meng, A stable and easily sintering BaCeO_3 -based proton-conductive electrolyte, *J. Alloys. Compd.* 473 (1–2) (2009) 323–329, <https://doi.org/10.1016/j.jallcom.2008.05.071>.
- Q. Wang, S. Ricote, M. Chen, Oxygen electrodes for protonic ceramic cells, *Electrochim. Acta* 446 (2023) 142101, <https://doi.org/10.1016/j.electacta.2023.142101>.
- W. Sun, Y. Jiang, Y. Wang, S. Fang, Z. Zhu, W. Liu, A novel electronic current-blocked stable mixed ionic conductor for solid oxide fuel cells, *J. Power. Sources.* 196 (1) (2011) 62–68, <https://doi.org/10.1016/j.jpowsour.2010.07.038>.
- B. Zhu, X. Liu, T. Schober, Novel hybrid conductors based on doped ceria and BCY20 for IT-SOFC applications, *Electrochem. Commun.* 6 (4) (2004) 378–383, <https://doi.org/10.1016/j.elecom.2004.01.015>.
- R. Raza, M.A. Ahmad, J. Iqbal, N. Akram, Z. Gao, S. Javed, B. Zhu, $\text{Ce}_{0.8}(\text{SmZr})_{0.2}\text{O}_2$ -carbonate nanocomposite electrolyte for solid oxide fuel cell, *Int. J. Energy Res.* 38 (4) (2014) 524–529, <https://doi.org/10.1002/er.3150>.
- A.V. Kuz'Min, V.P. Gorelov, N.V. Sharova, V.B. Balakireva, Phase transitions in the $\text{BaCe}_{1-x}\text{Nd}_x\text{O}_{3-\delta}$ system ($x=0-0.15$), *Russ. J. Electrochem.* 39 (2003) 454–460, <https://doi.org/10.1023/A:1023856322311>.
- X. Chi, J. Zhang, Z. Wen, Y. Liu, Modified Pechini synthesis of proton-conducting $\text{Ba}(\text{Ce}, \text{Ti})\text{O}_3$ and comparative studies of the effects of acceptors on its structure, stability, sinterability, and conductivity, *J. Am. Ceramic Soc.* 97 (4) (2014) 1103–1109, <https://doi.org/10.1111/jace.12742>.
- K. Katahira, Y. Kohchi, T. Shimura, H. Iwahara, Protonic conduction in Zr-substituted BaCeO_3 , *Solid. State Ion.* 138 (1–2) (2000) 91–98, [https://doi.org/10.1016/S0167-2738\(00\)00777-3](https://doi.org/10.1016/S0167-2738(00)00777-3).
- L. Bi, S. Zhang, L. Zhang, Z. Tao, H. Wang, W. Liu, Indium as an ideal functional dopant for a proton-conducting solid oxide fuel cell, *Int. J. Hydrogen. Energy* 34 (5) (2009) 2421–2425, <https://doi.org/10.1016/j.ijhydene.2008.12.087>.
- C.W. Tanner, A.V. Virkar, Instability of BaCeO_3 in H_2O -containing atmospheres, *J. Electrochem. Soc.* 143 (4) (1996) 1386, <https://doi.org/10.1149/1.1836647>.
- N. Zakovsky, S. Williamson, J.T. Irvine, Elaboration of CO_2 tolerance limits of $\text{BaCe}_{0.9}\text{Y}_{0.1}\text{O}_{3-\delta}$ electrolytes for fuel cells and other applications, *Solid. State Ion.* 176 (39–40) (2005) 3019–3026, <https://doi.org/10.1016/j.ssi.2005.09.040>.
- G. Ma, T. Shimura, H. Iwahara, Ionic conduction and nonstoichiometry in $\text{BaxCe}_{0.90}\text{Y}_{0.10}\text{O}_{3-\delta}$, *Solid. State Ion.* 110 (1–2) (1998) 103–110, [https://doi.org/10.1016/S0167-2738\(98\)00130-1](https://doi.org/10.1016/S0167-2738(98)00130-1).
- D.A. Medvedev, J.G. Lyagaeva, E.V. Gorbova, A.K. Demin, P. Tsiakaras, Advanced materials for SOFC application: strategies for the development of highly conductive and stable solid oxide proton electrolytes, *Prog. Mater. Sci.* 75 (2016) 38–79, <https://doi.org/10.1016/j.pmatsci.2015.08.001>.
- F. Zhao, Q. Liu, S. Wang, K. Brinkman, F. Chen, Synthesis and characterization of $\text{BaIn}_{0.3-x}\text{Y}_x\text{Ce}_{0.7}\text{O}_{3-\delta}$ ($x=0, 0.1, 0.2, 0.3$) proton conductors, *Int. J. Hydrogen. Energy* 35 (9) (2010) 4258–4263, <https://doi.org/10.1016/j.ijhydene.2010.02.080>.
- J. Dang, Z. Zhu, J. Qian, W. Liu, A stable $\text{BaCe}_{0.7}\text{Ta}_{0.1}\text{In}_{0.2}\text{O}_{3-\delta}$ electrolyte membrane for proton-conducting solid oxide fuel cells, *Ceram. Int.* 39 (4) (2013) 4287–4292, <https://doi.org/10.1016/j.ceramint.2012.11.008>.
- L. Bi, S. Zhang, S. Fang, Z. Tao, R. Peng, W. Liu, A novel anode supported $\text{BaCe}_{0.7}\text{Ta}_{0.1}\text{Y}_{0.2}\text{O}_{3-\delta}$ electrolyte membrane for proton-conducting solid oxide fuel cell, *Electrochem. Commun.* 10 (10) (2008) 1598–1601, <https://doi.org/10.1016/j.elecom.2008.08.024>.
- Y. Lin, R. Ran, Y. Zheng, Z. Shao, W. Jin, N. Xu, J. Ahn, Evaluation of $\text{Ba}_{0.5}\text{Sr}_{0.5}\text{Co}_{0.8}\text{Fe}_{0.2}\text{O}_{3-\delta}$ as a potential cathode for an anode-supported proton-conducting solid-oxide fuel cell, *J. Power. Sources.* 180 (1) (2008) 15–22, <https://doi.org/10.1016/j.jpowsour.2008.02.044>.
- E. Fabbri, L. Bi, D. Pergolesi, E. Traversa, High-performance composite cathodes with tailored mixed conductivity for intermediate temperature solid oxide fuel cells using proton conducting electrolytes, *Energy Environ. Sci.* 4 (12) (2011) 4984–4993, <https://doi.org/10.1039/c1ee02361f>.
- H. Zhang, F. Zhao, F. Chen, C. Xia, Nano-structured $\text{Sm}_{0.5}\text{Sr}_{0.5}\text{CoO}_{3-\delta}$ electrodes for intermediate-temperature SOFCs with zirconia electrolytes, *Solid. State Ion.* 192 (1) (2011) 591–594, <https://doi.org/10.1016/j.ssi.2010.05.024>.
- T. Wu, Y. Zhao, R. Peng, C. Xia, Nano-sized $\text{Sm}_{0.5}\text{Sr}_{0.5}\text{CoO}_{3-\delta}$ as the cathode for solid oxide fuel cells with proton-conducting electrolytes of $\text{BaCe}_{0.8}\text{Sm}_{0.2}\text{O}_{2.9}$, *Electrochim. Acta* 54 (21) (2009) 4888–4892.
- C. Duan, J. Tong, M. Shang, S. Nikodemski, M. Sanders, S. Ricote, R. O'Hayre, Readily processed protonic ceramic fuel cells with high performance at low temperatures, *Science* (1979) 349 (6254) (2015) 1321–1326, <https://doi.org/10.1126/science.aab3987>.
- J. Kim, S. Sengodan, G. Kwon, D. Ding, J. Shin, M. Liu, G. Kim, Triple-conducting layered perovskites as cathode materials for proton-conducting solid oxide fuel cells, *ChemSusChem.* 7 (10) (2014) 2811–2815, <https://doi.org/10.1002/cssc.201402351>.
- Y. Xia, Z. Jin, H. Wang, Z. Gong, H. Lv, R. Peng, L. Bi, A novel cobalt-free cathode with triple-conduction for proton-conducting solid oxide fuel cells with unprecedented performance, *J. Mater. Chem. A* 7 (27) (2019) 16136–16148, <https://doi.org/10.1039/C9TA02449B>.
- Z. Wei, J. Wang, X. Yu, Z. Li, Y. Zhao, J. Chai, Study on Ce and Y co-doped $\text{BaFeO}_{3.8}$ cubic perovskite as free-cobalt cathode for proton-conducting solid oxide fuel cells, *Int. J. Hydrogen. Energy* 46 (46) (2021) 23868–23878, <https://doi.org/10.1016/j.ijhydene.2021.04.188>.
- M. Liang, F. He, C. Zhou, Y. Chen, R. Ran, G. Yang, Z. Shao, Nickel-doped $\text{BaCo}_{0.4}\text{Fe}_{0.4}\text{Zr}_{0.1}\text{Y}_{0.1}\text{O}_{3-\delta}$ as a new high-performance cathode for both oxygen-ion and proton conducting fuel cells, *Chem. Eng. J.* 420 (2021) 127717, <https://doi.org/10.1016/j.cej.2020.127717>.
- H. Ding, W. Wu, C. Jiang, Y. Ding, W. Bian, B. Hu, D. Ding, Self-sustainable protonic ceramic electrochemical cells using a triple conducting electrode for hydrogen and power production, *Nat. Commun.* 11 (1) (2020) 1907, <https://doi.org/10.1038/s41467-020-15677-z>.
- A. Sultan, M. Ahmad, Z. Imran, S.S. Batool, K. Rasool, S. Hassan, M.A. Rafiq, Tailoring structural, dielectric and optical effects of PbS nanosheets with Ni doping, *Physica B* 602 (2021) 412571, <https://doi.org/10.1016/j.physb.2020.412571>.
- L. Bi, E. Fabbri, Z. Sun, E. Traversa, $\text{BaZr}_{0.8}\text{Y}_{0.2}\text{O}_{3-\delta}$ -NiO composite anodic powders for proton-conducting SOFCs prepared by a combustion method, *J. Electrochem. Soc.* 158 (7) (2011) B797, <https://doi.org/10.1149/1.3591040>.
- L. Bi, E. Fabbri, Z. Sun, E. Traversa, Sinteractive anodic powders improve densification and electrochemical properties of $\text{BaZr}_{0.8}\text{Y}_{0.2}\text{O}_{3-\delta}$ electrolyte films

- for anode-supported solid oxide fuel cells, *Energy Environ. Sci.* 4 (4) (2011) 1352–1357, <https://doi.org/10.1039/c0ee00387e>.
- [40] J. Tong, D. Clark, L. Bernau, M. Sanders, R. O'Hayre, Solid-state reactive sintering mechanism for large-grained yttrium-doped barium zirconate proton conducting ceramics, *J. Mater. Chem.* 20 (30) (2010) 6333–6341, <https://doi.org/10.1039/c0jm00381f>.
- [41] J. Tong, D. Clark, M. Hoban, R. O'Hayre, Cost-effective solid-state reactive sintering method for high conductivity proton conducting yttrium-doped barium zirconium ceramics, *Solid. State Ion.* 181 (11–12) (2010) 496–503, <https://doi.org/10.1016/j.ssi.2010.04.008>.
- [42] S. Ricote, N. Bonanos, Enhanced sintering and conductivity study of cobalt or nickel doped solid solution of barium cerate and zirconate, *Solid. State Ion.* 181 (15–16) (2010) 694–700, <https://doi.org/10.1016/j.ssi.2010.04.007>.
- [43] D. Montaleone, E. Mercadelli, A. Gondolini, M. Ardit, P. Pinasco, A. Sanson, Role of the sintering atmosphere in the densification and phase composition of asymmetric BCZY-GDC composite membrane, *J. Eur. Ceram. Soc.* 39 (1) (2019) 21–29, <https://doi.org/10.1016/j.jeurceramsoc.2018.01.043>.
- [44] A. Abdel Aal, T. Hammad, M. Zawrah, I. Battisha, A. Abou Hammad, FTIR study of nanostructure perovskite BaTiO₃ doped with both Fe³⁺ and Ni²⁺ ions prepared by sol-gel technique, *Acta Physica Polonica A* 126 (6) (2014) 1318–1321.
- [45] H. Shin, J. Seo, S. Jeon, S.J. Jeong, J. Kim, S. Lee, W. Jung, Enhanced catalytic activity and stability of SOFC electrodes through plasma-driven surface modification, *J. Mater. Chem. A* 12 (18) (2024) 10695–10703, <https://doi.org/10.1039/D3TA06111F>.
- [46] G. George, & S. Anandhan, Synthesis and characterisation of nickel oxide nanofibre webs with alcohol sensing characteristics, *RSC. Adv.* 4 (107) (2014) 62009–62020, <https://doi.org/10.1039/C4RA11083H>.
- [47] C. Lu, B. Niu, S. Yu, W. Yi, S. Luo, B. Xu, Y. Ji, Efficient and stable symmetrical electrode La_{0.6}Sr_{0.4}Co_{0.2}Fe_{0.7}Mo_{0.1}O_{3-δ} for direct hydrocarbon solid oxide fuel cells, *Electrochim. Acta* 323 (2019) 134857, <https://doi.org/10.1016/j.electacta.2019.134857>.
- [48] A.V. Naumkin, A.Y. Vasil'kov, Au-Ni and Au-Fe heterometallic systems: an X-ray photoelectron spectroscopy study, *Russ. Chem. Bulletin.* 62 (2013) 2559–2566, <https://doi.org/10.1007/s11172-013-0373-x>.
- [49] Q. Zeng, X. Zhang, W. Wang, D. Zhang, Y. Jiang, X. Zhou, B. Lin, A Zn-doped Ba_{0.5}Sr_{0.5}Co_{0.8}Fe_{0.2}O_{3-δ} perovskite cathode with enhanced ORR catalytic activity for SOFCs, *Catalysts.* 10 (2) (2020) 235, <https://doi.org/10.3390/catal10020235>.
- [50] K.R. Priolkar, P. Bera, P.R. Sarode, M.S. Hegde, S. Emura, R. Kumashiro, N.P. Lalla, formation of Ce_{1-x}Pd_xO_{2-δ} solid solution in combustion-synthesized Pd/CeO₂ catalyst: XRD, XPS, and EXAFS investigation, *Chem. Mater.* 14 (5) (2002) 2120–2128, <https://doi.org/10.1021/cm0103895>.
- [51] A. Kopia, K. Kowalski, M. Chmielowski, C. Leroux, Electron microscopy and spectroscopy investigations of CuO_x-CeO_{2-δ}/Si thin films, *Surf. Sci.* 602 (7) (2008) 1313–1321, <https://doi.org/10.1016/j.susc.2007.12.041>.
- [52] D. Xie, K. Li, J. Yang, D. Yan, L. Jia, B. Chi, J. Li, High-performance La_{0.5}(Ba_{0.75}Ca_{0.25})_{0.5}Co_{0.8}Fe_{0.2}O_{3-δ} cathode for proton-conducting solid oxide fuel cells, *Int. J. Hydrogen. Energy* 46 (15) (2021) 10007–10014, <https://doi.org/10.1016/j.ijhydene.2020.01.014>.
- [53] Q. Wang, J. Hou, Y. Fan, X.A. Xi, J. Li, Y. Lu, J.L. Luo, Pr₂BaNiMnO_{7-δ} double-layered Ruddlesden–Popper perovskite oxides as efficient cathode electrocatalysts for low temperature proton conducting solid oxide fuel cells, *J. Mater. Chem. A* 8 (16) (2020) 7704–7712, <https://doi.org/10.1039/C9TA11212J>.
- [54] B. Liu, J. Yang, D. Yan, L. Jia, B. Chi, J. Pu, J. Li, Novel PrBa_{0.9}Ca_{0.1}Co_{2-x}Zn_xO_{7+δ} double-perovskite as an active cathode material for high-performance proton-conducting solid oxide fuel cells, *Int. J. Hydrogen. Energy* 45 (55) (2020) 31009–31016, <https://doi.org/10.1016/j.ijhydene.2020.08.095>.
- [55] Z. Wang, J. Li, M. Yuan, J. Gao, H. Hao, A.M. Abdalla, B. Wei, A medium-entropy engineered double perovskite oxide for efficient and CO₂-tolerant cathode of solid oxide fuel cells, *Sustain. Mater. Technol.* 40 (2024) e00969.
- [56] X. Bao, Z. Wang, Z. Song, X. Chen, X. Su, X. Han, L. Zhang, Effects of high-valence Mo content on microstructure and properties of Ba₂Fe_{2-x}Mo_xO_{6-δ} anode materials for solid oxide fuel cells, *J. Alloys. Compd.* 976 (2024) 173271, <https://doi.org/10.1016/j.jallcom.2023.173271>.
- [57] J. Chen, D. Zhang, Y. He, L. Zhang, S. Wang, Enhanced electrochemical performance of SOFC: GDC electrolyte grains encapsulation via DZSB film, *Ceram. Int.* 50 (3) (2024) 5169–5178, <https://doi.org/10.1016/j.ceramint.2023.11.262>.
- [58] M. Dudek, B. Lis, R. Kluczowski, M. Krauz, M. Ziabka, M. Gajek, A. Raźniak, NiO–Ba_{0.95}Ca_{0.05}Ce_{0.9}Y_{0.1}O_{3-δ} as a modified anode material fabricated by the tape casting method, *Materials.* (Basel) 15 (7) (2022) 2489, <https://doi.org/10.3390/ma15072489>.
- [59] Y. Du, Y. Li, P. Ren, L. Zhang, D. Wang, X. Xu, Oxygen transfer at mesoscale catalyst layer in proton exchange membrane fuel cell: mechanism, model and resistance characterization, *Chem. Eng. J.* (2024) 153021, <https://doi.org/10.1016/j.cej.2024.153021>.
- [60] N. Porotnikova, D. Osinkin, Segregation and interdiffusion processes in perovskites: a review of recent advances, *J. Mater. Chem. A* 12 (5) (2024) 2620–2646, <https://doi.org/10.1039/D3TA06708D>.
- [61] H. Di, Z. Liu, M. Xiao, Y. Bai, G. Yang, Z. Luo, Z. Shao, Exploring hydration of air electrodes for protonic ceramic cells: a review, *Chem. Eng. J.* (2025) 160759, <https://doi.org/10.1016/j.cej.2025.160759>.
- [62] J. Kim, S. Sengodan, S. Kim, O. Kwon, Y. Bu, G. Kim, Proton conducting oxides: a review of materials and applications for renewable energy conversion and storage, *Renew. Sustain. Energy Rev.* 109 (2019) 606–618, <https://doi.org/10.1016/j.rser.2019.04.042>.
- [63] Y. Wan, Y. Xing, Z. Xu, S. Xue, S. Zhang, C. Xia, A-site bismuth doping, a new strategy to improve the electrocatalytic performances of lanthanum chromate anodes for solid oxide fuel cells, *Appl. Catal. B* 269 (2020) 118809, <https://doi.org/10.1016/j.apcatb.2020.118809>.
- [64] X. Luo, Y. Yang, Y. Yang, D. Tian, X. Lu, Y. Chen, B. Lin, Reduced-temperature redox-stable LSM as a novel symmetrical electrode material for SOFCs, *Electrochim. Acta* 260 (2018) 121–128, <https://doi.org/10.1016/j.electacta.2017.11.071>.
- [65] D. Tian, B. Lin, Y. Yang, Y. Chen, X. Lu, Z. Wang, E. Traversa, Enhanced performance of symmetrical solid oxide fuel cells using a doped ceria buffer layer, *Electrochim. Acta* 208 (2016) 318–324, <https://doi.org/10.1016/j.electacta.2016.04.189>.
- [66] L. dos Santos-Gómez, J.M. Porras-Vázquez, E.R. Losilla, D. Marrero-López, P. Slater, Investigation of PO₄³⁻ oxyanion-doping on the properties of CaFe_{0.4}Ti_{0.6}O_{3-δ} for potential application as symmetrical electrodes for SOFCs, *J. Alloys. Compd.* 835 (2020) 155437, <https://doi.org/10.1016/j.jallcom.2020.155437>.
- [67] J. Zhou, Y. Chen, G. Chen, K. Wu, Y. Cheng, Evaluation of La_xSr_{2-x}FeO₄ layered perovskite as potential electrode materials for symmetrical solid oxide fuel cells, *J. Alloys. Compd.* 647 (2015) 778–783, <https://doi.org/10.1016/j.jallcom.2015.05.261>.
- [68] Y. Zhang, H. Zhao, Z. Du, K. Świerczek, Y. Li, High-performance SmBaMn₂O_{5+δ} electrode for symmetrical solid oxide fuel cell, *Chem. Mater.* 31 (10) (2019) 3784–3793, <https://doi.org/10.1021/acs.chemmater.9b01012>.
- [69] C. Solís, L. Navarrete, F. Bozza, N. Bonanos, J.M. Serra, Catalytic surface promotion of composite cathodes in protonic ceramic fuel cells, *ChemElectroChem.* 2 (8) (2015) 1106–1110, <https://doi.org/10.1002/celec.201500068>.
- [70] J. Zhou, N. Wang, J. Cui, J. Wang, J. Yang, Z. Zong, K. Wu, Structural and electrochemical properties of B-site Ru-doped (La_{0.8}Sr_{0.2})_{0.9}Sc_{0.2}Mn_{0.8}O_{3-δ} as symmetrical electrodes for reversible solid oxide cells, *J. Alloys. Compd.* 792 (2019) 1132–1140, <https://doi.org/10.1016/j.jallcom.2019.04.103>.
- [71] V.D. Silva, R.M. Silva, J.P. Grilo, F.J. Loureiro, D.P. Fagg, E.S. Medeiros, D. A. Macedo, Electrochemical assessment of novel misfit Ca-cobaltite-based composite SOFC cathodes synthesized by solution blow spinning, *J. Eur. Ceram. Soc.* 38 (6) (2018) 2562–2569, <https://doi.org/10.1016/j.jeurceramsoc.2018.01.044>.
- [72] C.G. Lima, R.M. Silva, F.D.M. Aquino, B. Raveau, V. Caignaert, M.R. Cesario, D. A. Macedo, Proteic sol-gel synthesis of copper doped misfit Ca-cobaltite with potential SOFC application, *Mater. Chem. Phys.* 187 (2017) 177–182, <https://doi.org/10.1016/j.matchemphys.2016.11.063>.
- [73] Y. Yu, L. Yu, K. Shao, Y. Li, K. Maliutina, W. Yuan, L. Fan, BaZr_{0.1}Co_{0.4}Fe_{0.4}Y_{0.1}O_{3-δ} composite as quasi-symmetrical electrode for proton conducting solid oxide fuel cells, *Ceram. Int.* 46 (8) (2020) 11811–11818, <https://doi.org/10.1016/j.ceramint.2020.01.215>.
- [74] S.M. Babiniiec, S. Ricote, N.P. Sullivan, Infiltrated lanthanum nickelate cathodes for use with BaCe_{0.2}Zr_{0.7}Y_{0.1}O_{3-δ} proton conducting electrolytes, *J. Electrochem. Soc.* 161 (6) (2014) F717, <https://doi.org/10.1149/2.037406jes>.
- [75] A.P. Tarutin, M.Y. Gorshkov, I.N. Bainov, G.K. Vdovin, A.I. Vylkov, J.G. Lyagaeva, D.A. Medvedev, Barium-doped nickelates Nd_{2-x}Ba_xNiO_{4+δ} as promising electrode materials for protonic ceramic electrochemical cells, *Ceram. Int.* 46 (15) (2020) 24355–24364, <https://doi.org/10.1016/j.ceramint.2020.06.217>.
- [76] N. Danilov, J. Lyagaeva, G. Vdovin, E. Pikalova, D. Medvedev, Electricity/hydrogen conversion by the means of a protonic ceramic electrolysis cell with Nd₂NiO_{4+δ}-based oxygen electrode, *Energy Convers. Manage* 172 (2018) 129–137, <https://doi.org/10.1016/j.enconman.2018.07.014>.
- [77] J. Hou, J. Qian, L. Bi, Z. Gong, R. Peng, W. Liu, The effect of oxygen transfer mechanism on the cathode performance based on proton-conducting solid oxide fuel cells, *J. Mater. Chem. A* 3 (5) (2015) 2207–2215, <https://doi.org/10.1039/C4TA04397A>.
- [78] Y. Zhao, K. Zhang, Z. Wei, Z. Li, Y. Wang, Z. Zhu, T. Liu, Performance and distribution of relaxation times analysis of Ruddlesden–Popper oxide Sr₃Fe_{1.3}Co_{0.2}Mo_{0.5}O_{7-δ} as a potential cathode for protonic solid oxide fuel cells, *Electrochim. Acta* 352 (2020) 136444, <https://doi.org/10.1016/j.electacta.2020.136444>.
- [79] S. Wang, Y. Feng, D. Wang, Electrochemical comparison of cobalt-free La_{0.5}Sr_{0.5}Fe_{0.9}Mo_{0.1}O_{3-δ} based cathode materials for intermediate-temperature solid oxide fuel cells, *Ceram. Int.* 40 (4) (2014) 6359–6363, <https://doi.org/10.1016/j.ceramint.2013.10.133>.
- [80] S. Sun, Z. Cheng, SrCo_{0.8}Nb_{0.1}Ta_{0.1}O_{3-δ} based cathodes for electrolyte-supported proton-conducting solid oxide fuel cells: comparison with Ba_{0.5}Sr_{0.5}Co_{0.8}Fe_{0.2}O_{3-δ} based cathodes and implications, *J. Electrochem. Soc.* 167 (2) (2020) 024514, <https://doi.org/10.1149/1945-7111/ab6bba>.
- [81] C. Yang, X. Zhang, H. Zhao, Y. Shen, Z. Du, C. Zhang, Electrochemical properties of BaZr_{0.1}Ce_{0.7}Y_{0.1}Yb_{0.1}O_{3-δ}-Nd_{1.95}NiO_{4+δ} composite cathode for protonic ceramic fuel cells, *Int. J. Hydrogen. Energy* 40 (6) (2015) 2800–2807, <https://doi.org/10.1016/j.ijhydene.2014.12.084>.

- [82] A.R. Gilev, E.A. Kiselev, K.S. Sukhanov, D.V. Korona, V.A. Cherepanov, Evaluation of $\text{La}_{2-x}(\text{Ca/Sr})_x\text{Ni}_{1-y}\text{Fe}_y\text{O}_{4+\delta}$ ($x=0.5, 0.6$; $y=0.4, 0.5$) as cathodes for proton-conducting SOFC based on lanthanum tungstate, *Electrochim. Acta* 421 (2022) 140479, <https://doi.org/10.1016/j.electacta.2022.140479>.
- [83] L.A. Malik, A.A. Samat, A.M.M. Jani, Z. Jamil, N.H. Othman, C.J. Tseng, N. Osman, Electrode reaction routes analyses of modified Ni-BCZY anode via distribution relaxation times: 1-D interpretation, *Mater. Chem. Phys.* 333 (2025) 130353, <https://doi.org/10.1016/j.matchemphys.2024.130353>.
- [84] J. Wang, Z. Li, H. Zang, Y. Sun, Y. Zhao, Z. Wang, Q. Zheng, $\text{BaZr}_{0.1}\text{Fe}_{0.9-x}\text{Ni}_x\text{O}_{3-\delta}$ cubic perovskite oxides for protonic ceramic fuel cell cathodes, *Int. J. Hydrogen Energy* 47 (15) (2022) 9395–9407, <https://doi.org/10.1016/j.ijhydene.2022.01.012>.
- [85] W. Song, Z. Ma, Y. Yang, S. Zhang, X. Ou, Y. Ling, Characterization and polarization DRT analysis of direct ethanol solid oxide fuel cells using low fuel partial pressures, *Int. J. Hydrogen Energy* 45 (28) (2020) 14480–14490, <https://doi.org/10.1016/j.ijhydene.2020.03.146>.